Applied Mathematical Modelling 110 (2022) 633–662

Contents lists available at ScienceDirect

Applied Mathematical Modelling

journal homepage: www.elsevier.com/locate/apm

Propagation of large air pockets in ducts. Analytical and numerical approaches

Jorge Molina*, Pablo Ortiz

University of Granada, Esc. Ing. Caminos, Campus Fuentenueva, Granada 18071, Spain

ARTICLE INFO

Article history:
Received 11 February 2022
Revised 9 June 2022
Accepted 13 June 2022
Available online 16 June 2022

Keywords:
Air cavity propagation
Geysering
Interface dynamics
Two phase-flows
Continuous finite elements

ABSTRACT

This paper presents analytical and numerical methods to compute intrusion of air pockets and geysering events in sewer systems. The theoretical approach, accomplished by a control volume analysis, takes into account gas expansion effects and free surface position to determine impulsion of water above the bubble. This analytical model is able to predict dynamics of single and consecutive elongated rising bubbles, revealing conditions that contribute to a sudden bubble decompression, and therefore to a severe geysering event. A non-oscillatory finite element method (NFEM) for fluid interface flows is the basis to construct the numerical model. The method assures positivity of phase function, reduces spurious momentum transfers between phases, and integrates a modified continuity equation to preserve mass under the weak compressibility assumption. Numerical simulations scrutinize conditions for emergence of air pockets in ducts, giving rise to simple solutions that provide the required flow rate to avoid the intrusion of cavities. Axisymmetric and complete three dimensional numerical models are used to perform rising Taylor bubbles and geysering experiments, to complement analytical results by giving precise flow details, in particular above the ground level.

1. Introduction

A relevant problem associated with urban sewer systems and storm-water storages is their saturation due to heavy rainfall events and the subsequent intrusion and propagation of large air pockets in ducts. Air pockets normally propagate in contact with the atmosphere, but they can become sealed due to the presence of obstacles, duct slopes, section changes, and flow rate increases. If a closed traveling air pocket finds a saturated vertical shaft, the resulting elongated rising bubble (or Taylor bubble) is able to drive the still water, returning fluid to the ground level and originating a geyser (see frames from a footage of a real geyser in Fig. 21). We primarily focus on initial and last stages, these ones being the most determinant factors linked to geysering phenomena. Thus, on the one hand, concerning initial stages, we conducted an original research on flow conditions that avoid the intrusion of air pockets in saturated ducts. These conditions are scrutinized through numerical simulations, and, moreover, we propose straightforward semi-analytical expressions fitting results of numerical experiments. On the other hand, concerning the last stages of propagation, a novel semi-analytical model for rising Taylor bubbles is presented to predict cavity dynamics inside vertical ducts and to evaluate configurations that lead to strong geysering events.

* Corresponding author.
E-mail addresses: jorgemolina@ugr.es (J. Molina), portiz@ugr.es (P. Ortiz).

https://doi.org/10.1016/j.apm.2022.06.016

Intrusion and propagation of open air cavities have been studied during the last decades mainly by experimental resources (see e.g. Refs. [1,2]). Nevertheless, recent works in the subjects have additionally employed simplified numerical approximations to reproduce the cavity's dynamics (see e.g. Ref. [3]). In the same way, current investigations concerning entrapped air pockets have resorted to simplified mathematical models as the rigid column model [4] or the elastic water column model [5] to scrutinize their effects on hydraulic structures. Numerical approximations have been also applied to this end, most of them based on the Volume of Fluid method (see e.g. Refs. [6,7]). Reader can consult Ref. [8] for an up-to-date state of the art. In the present work, an advanced semi-analytical approach and an ad-hoc finite element-based model are formulated to reproduce and to assess all propagation stages of air cavities, comprising geysering events. The ad-hoc continuous finite element model addresses the current multiphase flow problem. The method can be categorized as an interface capturing algorithm (see Ref. [9] and references therein for a comprehensive review), and follows the idea of the conservative level set method [10,11] by reconstructing interface sharpness in a reinitialization step [12]. The present approach, unlike other numerical models employed to simulate air pockets and bubbles (see e.g. Ref. [13]), also incorporates a weak-compressibility assumption to adequately represent gas expansion processes. Equations of motion for two weakly compressible fluids [14] are solved by coupling interface dynamics and physical properties through a transport equation for a bounded phase function. Continuity equation is properly modified to preserve mass conservation under the assumption of nearly incompressible flows. Moreover, a non-oscillatory finite element method (NFEM) [15–17] is employed for two purposes: first, to preserve positivity of phase function after advection and reinitialization steps; second, to prevent spurious momentum transfers between phases [18]. In the present work three levels of the numerical model are implemented, a two-dimensional version, an axisymmetric approximation, and a full three-dimensional form. Numerical model is concisely reported in section 2 and Appendix A, once governing equations for flow of two nearly incompressible fluids are established. Full information on the formulation of the numerical technique for fluid interface propagation is provided in Ref. [14].

We explore the first propagation stage of an air cavity to elucidate and get new insights of the minimum flow velocity that prevents intrusion of air in a conduit with a partially closed gate at its end (see sketch in Fig. 1). This configuration can be recognized in several experimental works (e.g. Ref. [19]). However, unlike previous studies where fluid inside the duct is at rest, a more realistic hypothesis is here assumed by imposing an initial fluid flow. Thus the experiment resembles a real sewer system under a rainfall event. Experiments of air cavity emergence are produced with the numerical model, establishing minimum flow velocity and its dependence on gate height and duct slope. Besides, we also propose in this work simple equations to calculate the required flow rate that accurately predict numerical outputs. Section 3 reports tests and results.

A new semi-analytical model examines Taylor bubbles dynamics. Existing approaches currently assume a conduit with semi-infinite length and potential flow around the bubble (see e.g. Refs. [20,21]). In this work the semi-analytical model is based on an integral analysis and it is performed without resorting to simplified bubble shapes (for example Ref. [22]). Besides, the formulation takes into account free surface position as well as the effect of gas expansion over bubble rising velocity. The resulting set of equations predicts the bubble rising dynamics. Furthermore, the set of equations allows the definition of a novel analytical condition to foresee the sudden decrease of the bubble's inner pressure, that produces a huge bubble acceleration and, therefore, a severe ejection of water to the street level. Assessment of the model is carried out by comparing theoretical outcomes with existing laboratory results. Next, we extend the semi-analytical approach to multiple rising bubbles, with the aim of scrutinizing the impact of trailing bubbles on the leading one, and vice versa. Section 4 covers the complete formulation of the semi-analytical model as well as a thorough appraisal and discussion, while Appendix B reports the solution algorithm proposed.

Section 5 focusses on numerical experiments. The aim of the experiments is twofold. The first series of tests estimates the limits of semi-analytical approach to multiple bubbles dynamics, by comparing theoretical predictions with numerical outputs. For this purpose, we simulate two consecutive bubbles rising in a vertical duct, and scan free surface and bubbles positions on time. Numerical model reveals flow features not captured by theoretical equations, such as detachment of small bubbles and its influence over trailing bubble. The second series of tests evaluates a closed air cavity propagating along a conduit connected with ground level through a vertical saturated shaft. Unlike other numerical studies (e.g. Ref. [7]) we also include in the numerical domain a portion of the street level to capture the geyser's characteristics. As a result of the three-dimensional simulation of a complete system (nearly-horizontal and vertical conduits), it is feasible to carry out a comprehensive examination of the air mass and momentum transfer from a (nearly) horizontal flow to the vertical duct, as well as the impulsion of still water that causes the final geyser. Conclusions in section 6 close the paper.

2. Governing Equations and Numerical Model

Conservation equations for flow of two nearly incompressible fluids is written as,

$$\frac{\partial \rho}{\partial t} + \nabla \cdot (\rho \mathbf{u}) = 0\,, \tag{1}$$

$$\frac{\partial \mathbf{u}}{\partial t} + \nabla \cdot (\mathbf{u}\mathbf{u}) = -\frac{1}{\rho}\nabla p + \frac{1}{\rho}\nabla \cdot \tau + \mathbf{g} + \mathbf{T} + \mathbf{Q}, \tag{2}$$

in the domain Ω with boundary Γ, and in the time interval $t \in [t_0, T]$. Here, $\mathbf{u}$ is the velocity field, p is the pressure, τ is the viscous stress tensor, $\mathbf{g}$ is the acceleration of gravity, $\mathbf{T}$ is the surface tension term, and $\mathbf{Q} = \mathbf{u}(\nabla \cdot \mathbf{u})$. Interface capture

is accomplished by advecting a continuous phase function $\phi \in [0, 1]$, such that $\phi=1$ in the domain occupied by the heavier fluid, $\phi=0$ in the domain occupied by the lighter fluid and $\phi=1/2$ on the interface. Thus, along with the fluids motion equations, the transport equation

$$\frac{\partial \phi}{\partial t} + \nabla \cdot (\mathbf{u}\phi) = 0 \quad \text{in } \Omega\,,\ t \in [t_0, T] \tag{3}$$

is integrated to achieve phase function solution.

Flows studied in numerical experiments are subjected to small pressure variations. Then, though real polytropic coefficient is unknown, density changes are similar under isothermal and adiabatic conditions, and error in density computations is small, independently of the hypothesis adopted. In case of the numerical approach, flows are assumed isothermal [23]. Hence, the density variation is a consequence of an elastic deformation due to the pressure change, $\rho \approx \rho(p_0) + \frac{p - p_0}{a^2}$, where p_0 is the reference pressure, $a = \sqrt{\mathcal{K}/\rho}$ is the acoustic wave velocity, and $\mathcal{K}$ is the elastic bulk modulus. Density and viscosity are defined by the phase function as

$$\rho = \rho_1 + (\rho_2 - \rho_1)\phi + \frac{p - p_0}{a_1^2 + \left(a_2^2 - a_1^2\right)\phi}, \tag{4}$$

$$\mu = \mu_1 + (\mu_2 - \mu_1)\phi, \tag{5}$$

where sub-indexes 1 and 2 indicate properties of the lighter and heavier fluid respectively. Variation of viscosity due to pressure modification is assumed negligible. Surface tension force is simulated using the approximation proposed in Ref. [24]. The equivalent surface tension volume force is

$$\mathbf{T} = \frac{2\sigma}{\rho_1 + \rho_2}\kappa \frac{\nabla \rho}{(\rho_2 - \rho_1)}\,, \tag{6}$$

where σ is the surface tension coefficient and $\kappa = -\nabla \cdot \frac{\nabla \phi}{|\nabla \phi|}$ is the interface curvature. Now, by introducing Eq. (4) into Eq. (1) and taking into account the phase function advection equation (3), continuity equation (1) results in

$$\frac{\partial}{\partial t}\left(\frac{p - p_0}{a_1^2 + (a_2^2 - a_1^2)\phi}\right) + \nabla \cdot \left(\rho' \mathbf{u}\right) = 0\,, \tag{7}$$

where $\rho' = \rho_1 + \frac{p - p_0}{a_1^2 + (a_2^2 - a_1^2)\phi}$.

Numerical solution of the continuous model given by Eqs. (2), (7), and (3) is performed by the non-oscillatory finite element method designated as NFEM [12,14]. The model is founded on the flux corrected transport (FCT) method (see Ref.[15] and references therein). The NFEM corrects a conservative, low order and sign-preserving predictor solution by anti-diffusive fluxes. Final solution maintains properties of the low order approach but ameliorates its large diffusion error. Correction fluxes are calculated by modifying differences between contributions of the low order predictor and those of a conservative high order solution. The reader can see details on formulation of flux correction principles in Ref. [17]; for NFEM simulations of flows with evolutionary boundaries, see Ref. [25].

The non-oscillatory finite element method solves equations of flow motion and phase transport. In regard to phase advection, NFEM provides a positive-definite solution. Although NFEM reduces significantly the amount of extra-diffusion coming from the low order algorithm, reinitialization of the phase function is necessary to preserve resolution of the contact discontinuity. Reinitialization step controls the region where phase function takes values between zero and one (interface width), and is performed by a non-linear anisotropic diffusion equation,

$$\frac{\partial \hat{\phi}}{\partial \tau} = \frac{\partial}{\partial \mathbf{n}}\left[K\left(\hat{\phi}\right)\frac{\partial \hat{\phi}}{\partial \mathbf{n}}\right], \tag{8}$$

$$K\left(\hat{\phi}\right) = \varepsilon - \frac{\hat{\phi}\left(1 - \hat{\phi}\right)}{\frac{\partial \hat{\phi}}{\partial \mathbf{n}} + \varsigma}\,, \tag{9}$$

where $\hat{\phi}$ is the reconstructed phase function, $\mathbf{n}$ is the interface normal and diffusion parameter $K(\hat{\phi})$ comprises the effects of an artificial compression balanced with an streamline diffusion. Here, τ is a dummy time variable, and ς is a small number to avoid the vanishing of the denominator. Parameter ε specifies the amount of diffusion and is proportional to the interface thickness η according to $\eta \approx 6\varepsilon$ (see Ref. [11], pp 796). Besides, the reinitialization step avoids discontinuities in phase function and, ultimately, in density and viscosity.

The NFEM also alleviates spurious momentum transfers between phases in the two fluids flow solution. However, for interfaces with very low density ratio ρ_1/ρ_2, standard flux correction procedure can not completely get rid of spurious velocity jumps. To address this problem, anti-diffusion fluxes are calculated with customized bounds that take into account the interface location (see details in Ref. [12]). The modified procedure proves to be beneficial for low density ratio

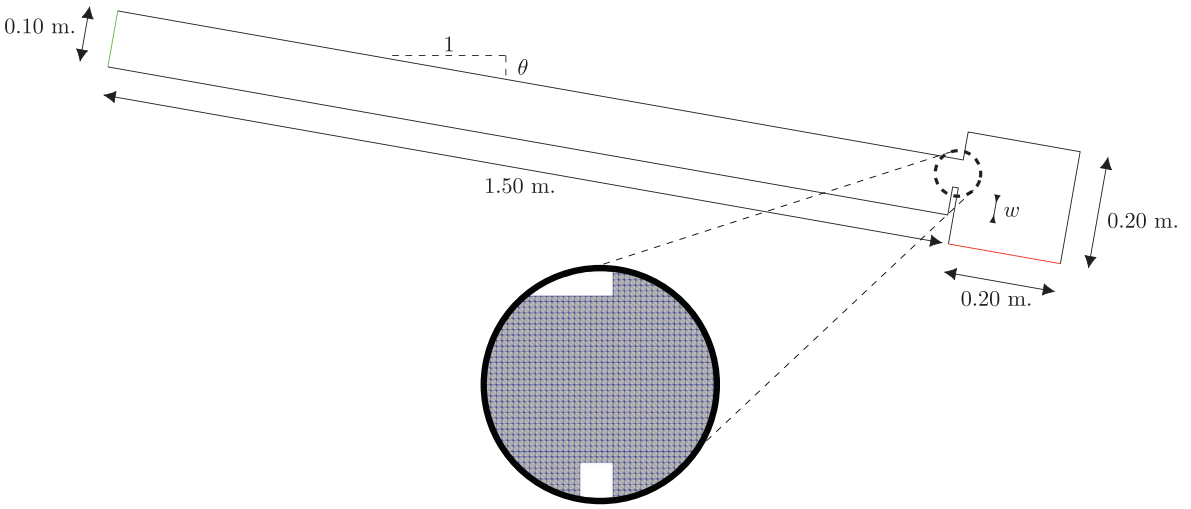

Fig. 1. Domain for air cavities simulations and detail of the mesh. Black color boundary: slip condition; green color boundary: inlet condition; red color boundary: inlet/outlet condition.

simulations without distorting the interface dynamics (see numerical experiments in Refs. [12,14]). High order solution of Eqs. (7) and (2) is attained by the characteristic based split finite element method (CBS). This method uses the well-known fractional step idea (see e.g. Ref. [26]). Low order algorithm in the NFEM for flow solution is, as in advection step, a finite element upwind method. The low order algorithm follows the same fractional steps as the high order algorithm and, consequently, computation of high and low order approaches demand solution of two Poisson equations each timestep. This double computation is circumvented by implementing a cost-effective algorithm, performing velocity correction only for the predictor velocity field. All series of experiments have shown that the use of this abridged method instead of the monolithic NFEM does not give noticeably different results, while computational cost is reduced around 40-50%. High and low order finite element solutions of Eqs. (7), (2) and (3), in addition to the flux correction technique, are summarized in Appendix A, whereas the extended solution procedure and details can be scrutinized in Refs. [12,14].

3. Air Intrusion Conditions

An usual arrangement to simulate air cavity propagation, either by laboratory or by numerical model, is as follows. First, a horizontal or nearly horizontal duct is filled with a liquid (generally water), and includes a gate located across its end (see sketch in Fig. 1). Second, a large air pocket intrudes into the duct from the open or partially open end and propagates upwards. Third, the air cavity finds a saturated vertical tube (at left of Fig. 1, not plotted), resulting in a rising bubble able to drive the still water (as Fig. 6), and eventually able to generate a geyser at street level (see as illustration Fig. 5.2b). Although these configurations are beneficial to compare analytical and numerical results with laboratory observations, they do not consider cases imitating real floods. In these cases, air cavities are superimposed on the flows that cause pressurization of the conduit. In this section we take into consideration these real states, and explore flow conditions under which air is not allowed to enter inside the conduit.

A series of tests is conducted with the numerical model reported in section 2. The domain consists of a rectangular duct of length 1.50 m and height D=0.10 m, a gate of variable height situated at the right end, and a chamber of 0.20×0.20 m to drain the water (Fig. 1). Water and air flows are assumed as nearly-incompressible, air density ρ_1=1.205 kg/m^3, dynamic viscosity $\mu_1 = 1.808 \cdot 10^{-5}$ kg/(ms) and sound speed squared $a_1^2 = 1.0 \cdot 10^5 \text{m}^2/\text{s}^2$. Water density ρ_2=998 kg/m^3, dynamic viscosity $\mu_2 = 1.0 \cdot 10^{-3}$ kg/(ms) and sound speed squared $a_2^2 = 2.2 \cdot 10^6$ m^2/s^2; surface tension parameter σ=0.07 N/m, and gravity $|\mathbf{g}|$=9.81 m/s^2. Average element lengths[1] for the numerical experiments were selected according to previous tests reported in Ref. [14]. In that work, grid studies were evaluated for demanding practical problems with several similarities with the problems considered in the present work, such as dam breaking flow with obstacles and, indeed a simplified treatment of air cavities for horizontal ducts. Reader can consult this reference for further information about the importance of mesh resolution and reinitialization process in the precision of the interface tracking. In this case, we employ a structured linear triangular finite element grid with average element length $\delta = 1.67\sqrt{2} \cdot 10^{-3}$ m. The time step $\Delta t \in \left[1 \cdot 10^{-4}, 1 \cdot 10^{-5}\right]$ s. Numerical parameters values for reinitialization stage are: amount of diffusion $\varepsilon = 0.83\Delta l$ and dummy time step $\Delta\tau = 0.1\Delta l^2/(8\varepsilon)$, where Δl is the maximum element length. Finally, parameter Υ prevents creation of new limits across the interfaces during flux correction process [12]; $\Upsilon = \Delta l/(600\varepsilon)$ proves to be adequate to alleviate

[1] Average element length for 2D structured meshes is $\delta = \sqrt{\Delta x^2 + \Delta y^2}$.

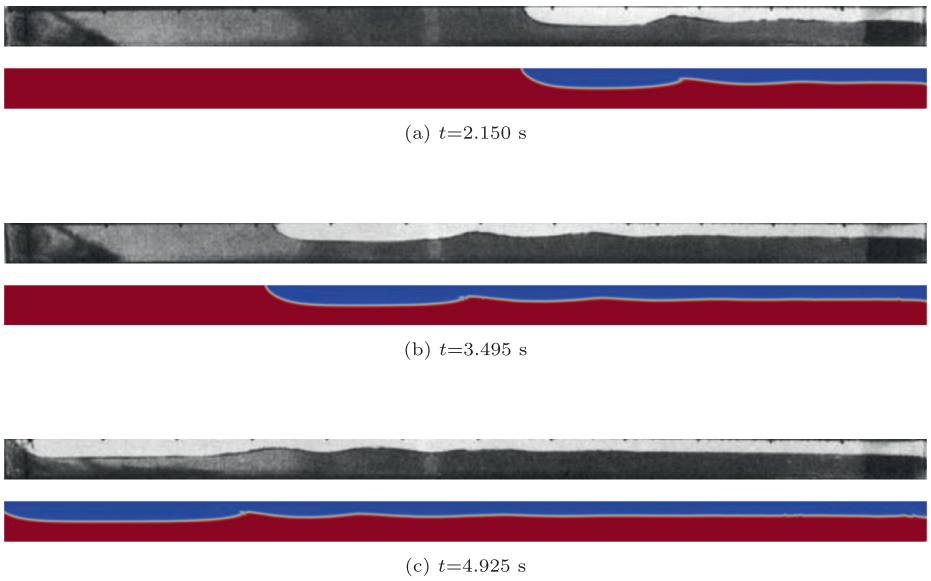

Fig. 2. Comparison of the cavity's shape for laboratory (top plots) and numerical (bottom plots) experiments with a similar setup. Source of laboratory results: Ref. [2], Figure 1.

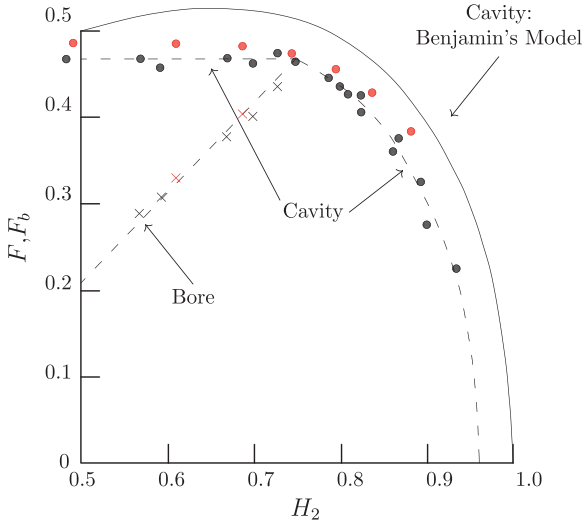

Fig. 3. Cavity and bore normalized celerities as function of downstream water depth ratio. Red marks: numerical results; black marks: experimental [2]. Solid line: theoretical [1]; dashed line: theoretical [2]. $F = c/\sqrt{gD}$, $F_b = c_b/\sqrt{gD}$, $H_2 = h_2/D$, c_b is the bore celerity and h_2 is the flow depth downstream the bore.

spurious momentum transfers between air and thin water layers attached to duct wall. Slip boundary condition is applied on solid walls (black in Fig. 1). On inlet/outlet boundary (red in Fig. 1) velocity is free, p=0, $\partial p/\partial \mathbf{n}_b$=0, and ϕ=0, where $\mathbf{n}_b$ is the outward normal to the boundary; hence if $\mathbf{u}\cdot\mathbf{n}_b$ <0, air flows into the domain. Phase function and velocity are prescribed on inlet boundary (green in Fig. 1) to reproduce water inflow. As initial condition, duct is filled up with still water in all cases. Simulations are specified by varying gate height w and duct slope θ. Every run last for 3 s.

Firstly we reproduce the experiment of D.L. Wilkinson [2], where the duct is horizontal and water inflow is zero. Tests were conducted for gate heights w/D=0.0, 0.2, 0.3, 0.4, 0.5, 0.6 and 0.7. Under these conditions a bore with low supercritical Froude number is developed downwind the front of the cavity as can be seen in Fig. 2, where cavity's shape obtained in Ref. [2] is compared with that given by our numerical model for three different time instants. As can be noted, the implemented finite element model is able to capture the free surface's dynamics fairly well.

Besides, Fig. 3 depicts results of D.L. Wilkinson superimposed with our numerical outputs. The figure plots the normalized cavity celerity $F = c/\sqrt{gD}$, where c is the cavity celerity, and normalized bore celerity $F_b = c_b/\sqrt{gD}$, where c_b is the bore celerity, in terms of downstream water depth ratio $H_2 = h_2/D$; the depth h_2 is measured downstream the bore. Black

Fig. 4. Conduit with w/D=0.2, θ=2% and u_w=0.35 m/s. Numerical results at t=3 s.

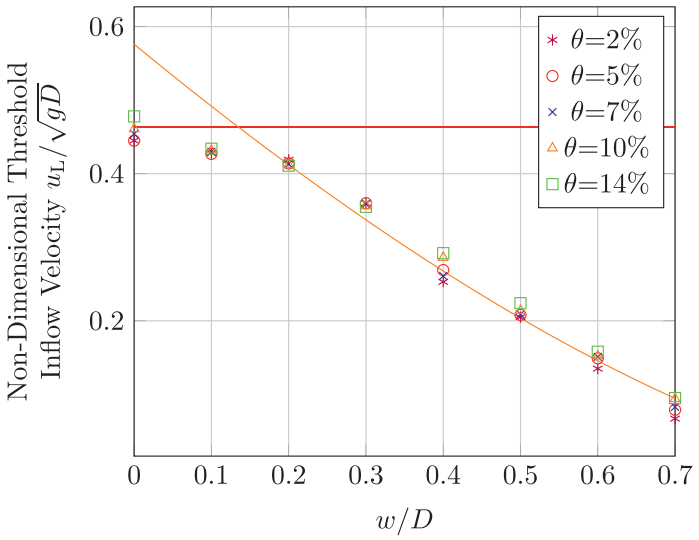

Fig. 5. Inflow velocity limit value as function of gate height w and slope θ. Red line is the velocity of a cavity unaffected by the bore (see Ref. [2]). Orange line is $u_L/\sqrt{gD}$=0.611$\frac{2}{3}\sqrt{2}(1-w/D)^{3/2}$.

marks indicate experimental measurements in Ref. [2], and red marks indicate numerical outputs; cross sign corresponds to bore celerity, while circle sign corresponds to cavity celerity. Finally, solid line represents the historical theoretical results by Benjamin [1], and dashed lines represent theoretical results in Ref. [2], taking into account surface tension and stagnation point position effects. Numerical results are slightly higher than measurements, but these differences are always less than 5% compared with laboratory results. Besides, for unsteady regime (i.e., when bore and cavity have different celerities), results of bore celerities are in good agreement with measurements.

Now, the main goal is to determine the threshold inflow velocity u_L, such that air does not intrude into the conduit. For each pair w, θ several inlet velocities are tested. The strategy is: first, to select those simulations such that air is present inside the duct at last time step; second, to calculate mean gas inflow rate over the whole computational time; third, to get inlet velocity limit value for which gas inflow rate is zero by linear regression (a sound method, based on test comparisons). Experiments were performed for w/D=0.0, 0.1, 0.2, 0.3, 0.4, 0.5, 0.6, 0.7; and for θ=2%, 5%, 7%, 10%, 14%. As an example, in Fig. 4 we plot the numerical results at 3 s for a conduit with w/D=0.2, θ=2% and inlet velocity u_w=0.35 m/s. Reader can check the effect of the incoming flow by comparing this output with that showed in Fig. 2a. Fig. 5 depicts the non-dimensional limiting inflow velocity in terms of w/D for the slopes selected. A low dependence of threshold velocity on moderate slopes is manifest. Analytical solutions of cavity and bore propagation celerities in stagnant fluid are reported in Ref. [2]. In case of an uniform liquid flow in the conduit with an average velocity u_w, the analytical calculation of celerities is modified in a simple manner. As a result, if flow velocity equals analytical cavity celerity in stagnant fluids $c = 0.464\sqrt{gD}$ (see Ref. [2]), such that $u_w = c$, air pocket does not propagate inside the duct. This straightforward theory is only valid for low gate heights (w/D<0.1, see red line in Fig. 5 representing simplified theory, and compare it with numerical (points)). For gates in higher positions (w/D>0.1), to establish a theoretical threshold inflow velocity, it is sufficient to calculate the flow rate over the gate if interface is in contact with upper duct wall,

$$q = \frac{2}{3} C_d \sqrt{2g}(D-w)^{3/2},$$

where q is the flow rate per unit width and C_d is the gate discharge coefficient. Hence, if $u_w D \geq q$, air flow rate is zero, so

$$u_L/\sqrt{gD} = \frac{2}{3} C_d \sqrt{2}(1-w/D)^{3/2}. \tag{10}$$

The orange curve in Fig. 5 represents Eq. (10) for C_d=0.611. It is apparent that the numerical model approximates the analytical solutions accurately for the whole range of gate openings.

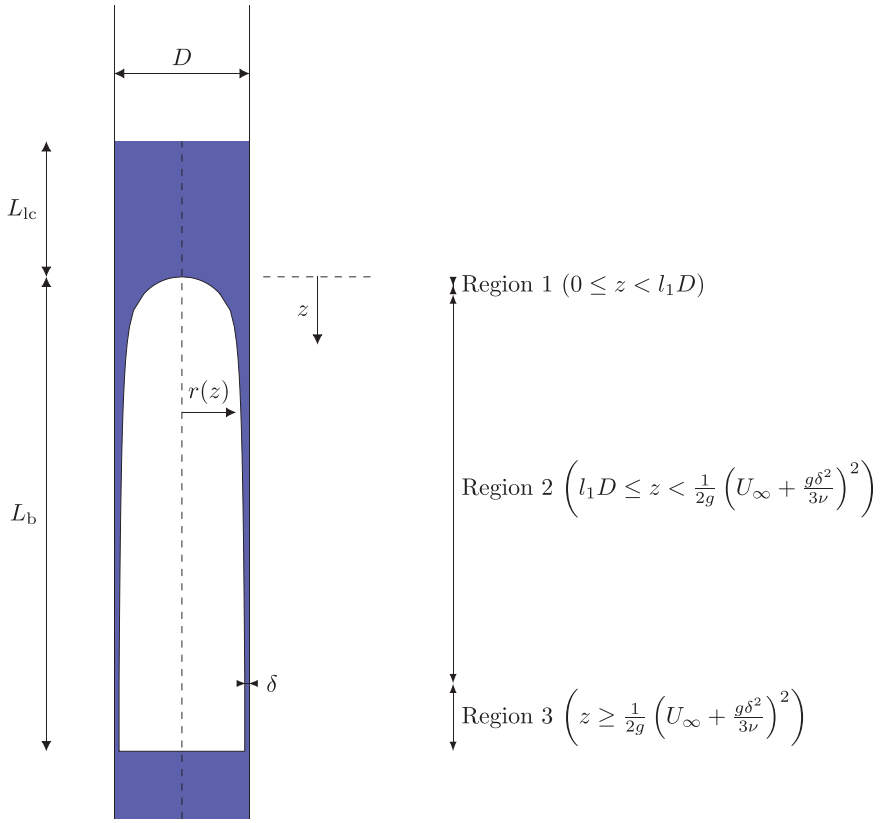

Fig. 6. Sketch of a rising bubble.

4. Semi-Analytical Approach of Geysering Phenomena due to Elongated Bubbles

In this section we study the effect of rising Taylor bubbles on the liquid free surface in a vertical duct (Fig. 6). Firstly we examine the case with a single bubble; secondly we extend the formulation to several consecutive bubbles. In the study presented in Ref. [22] bubble shape was simplified and drift velocity was imposed as initial bubble velocity. Here, we consider a realistic bubble shape and take into account drag force, buoyancy force, and gas expansion effect to calculate bubble dynamics.

4.1. Single Bubble Geometry

Fig. 6 sketches a single Taylor bubble rising in a circular vertical tube with diameter D. Bubble shape is established for three regions [27],

$$r(z) = \begin{cases} \frac{1}{2}\sqrt{z(3D-4z)} & \text{if} \quad 0 \le z < z_1 \\ \frac{D}{2}\sqrt{1-\frac{U_\infty}{\sqrt{2gz}}} & \text{if} \quad z_1 \le z \le z_2 \\ \frac{D}{2}-\delta & \text{if} \quad z > z_2 \end{cases}, \tag{11}$$

where r and z are the radial and vertical coordinates, respectively (Fig. 6), and g is the gravity acceleration. Bubble in the first region has spherical shape with radius $3D/8$. In the second region, bubble shape is obtained under the premise of constant air pressure by applying mass conservation and Bernoulli equation along a streamline passing by bubble nose. Bubble velocity in stagnant liquid U_∞ is defined as,

$$U_\infty = k\sqrt{gD}, \tag{12}$$

where k is a non-dimensional constant. The value of the constant was reported in Refs. [28] and [29], among others, and k=0.345 is the commonly used value. In the third region viscous force dominates, and there δ designates the liquid film

thickness between bubble and duct wall. Following Ref. [30], thickness δ can be calculated from the equation

$$U_\infty \pi \frac{D^2}{4} = \left(U_\infty + \frac{g\delta^2}{3\nu}\right) \cdot (\pi\,\delta\,(D-\delta))\,, \tag{13}$$

where ν is the kinematic viscosity of the liquid. Equation (13) establishes conservation of mass for a moving control volume that embraces zones 1 and 2 of the Taylor bubble (see Fig. 6) and the surrounding liquid, where a parabolic velocity profile is assumed across the liquid layer with thickness $\delta \ll D/2$ between the bubble interface and the solid wall. Note that this assumption does not imply that velocity at the bubble interface is zero. Intake liquid flow rate in the control volume through the upper boundary is the left hand side of Eq. (13), while outflow rate through the lower boundary is the right hand side of Eq. (13). The thickness of the liquid layer and the liquid mean velocity were measured in Ref. [31]. Authors found that, although theoretical models overestimate the mean velocity and underestimate the film thickness, flow rate obtained with the right hand side of Eq. (13) was in close agreement with experimental results.

The limit z_1 in Eqs. (11) can be attained by equating first shape equation with second shape equation (Eqs. (11)), leading to $z_1 = l_1(k)D$. For k=0.345, l_1=0.128484. A similar course of action is taken to get z_2, resulting in

$$z_2 = \frac{1}{2g}\left(U_\infty + \frac{g\delta^2}{3\nu}\right)^2 . \tag{14}$$

Last equation derives from equating mathematical expressions for zones 2 and 3 in Eq. (11) and considering Eq. (13).

To complete geometry information required in next section, the bubble volume and the surrounding liquid volume are calculated by Eqs. (11). Moreover, we specify the derivative of the gas volume confined in the bubble respect to the vertical coordinate. Bubble volume $V = \int_0^{L_b} \pi r^2(z)\,\mathrm{d}z$. Then, if $L_b \geq z_2$,

$$V = \frac{\pi}{4}D^3 l_1^2\left(\frac{3}{2} - \frac{4}{3}l_1\right) + \frac{\pi D^2}{4}\left[(z_2 - l_1 D) - k\sqrt{2D}\left(\sqrt{z_2} - \sqrt{l_1 D}\right)\right] + \pi\left(\frac{D}{2} - \delta\right)^2 (L_b - z_2)\,, \tag{15}$$

where L_b is the bubble height (Fig. 6), while if $z_1 < L_b < z_2$, volume is

$$V = \frac{\pi}{4}D^3 l_1^2\left(\frac{3}{2} - \frac{4}{3}l_1\right) + \frac{\pi D^2}{4}\left[(L_b - l_1 D) - k\sqrt{2D}\left(\sqrt{L_b} - \sqrt{l_1 D}\right)\right].$$

Surrounding liquid volume V_l is

$$V_l = \frac{\pi D^2}{4}\left[Dl_1 - Dl_1^2\left(\frac{3}{2} - \frac{4}{3}l_1\right) + k\sqrt{2D}\left(\sqrt{z_2} - \sqrt{l_1 D}\right)\right] + (L_b - z_2)\pi\,\delta\,(D-\delta)\,. \tag{16}$$

Lastly, derivative of gas volume $V_g = V$ respect to z is

$$\frac{\mathrm{d}V_g}{\mathrm{d}z} = \begin{cases} \pi\frac{D^2}{4}\left(1 - \frac{k\sqrt{D}}{\sqrt{2z}}\right) & \text{if} \quad z_1 < L_b < z_2 \\ \pi\left(\frac{D}{2} - \delta\right)^2 & \text{if} \quad L_b \geq z_2 \end{cases}, \tag{17}$$

4.2. Compressibility Model

Liquid with density ρ_l surrounding the bubble is incompressible, and gas compression and expansion are assumed adiabatic. This assumption is commonly used in problems involving two phase flows into ducts (see e.g. Refs. [22,32,33]), and error committed is negligible if pressure changes are small. Then, gas density is given by

$$\rho_g = \left(\frac{P + P_{atm}}{C}\right)^{1/\gamma} ; \quad C = \frac{P_{atm}}{\rho_{g0}^{\gamma}}\,, \tag{18}$$

where P is the relative gas pressure, P_{atm} is the atmospheric pressure, γ is the gas adiabatic index and ρ_{g0} is the gas density at atmospheric pressure.

4.3. Control Volume Analysis

Analysis of a single rising bubble in a vertical conduit is accomplished by applying integral form of conservation equations to the bubble and to the liquid situated above the gas. We consider the problem as one-dimensional, including only motion along vertical axis. The liquid column below the bubble is assumed to be much greater than the liquid column above the bubble; hence gas expansions or compressions only have an effect on the upper region of the bubble (in agreement with conclusions in Ref. [34]). Besides, consistent with these premises, free surface height perturbations ascribed to the rise of a hypothetical incompressible bubble are considered much smaller than those perturbations ascribed to bubble velocity changes caused by gas expansion/compression processes, and then former perturbations are neglected. This assumption was corroborated by means of a numerical test in which the air was assumed incompressible. Results showed that free surface,

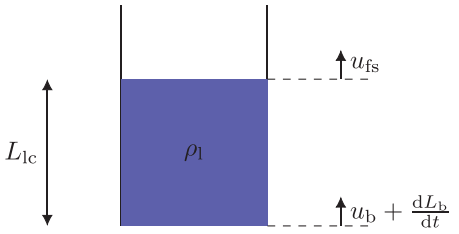

Fig. 7. Control Volume 1.

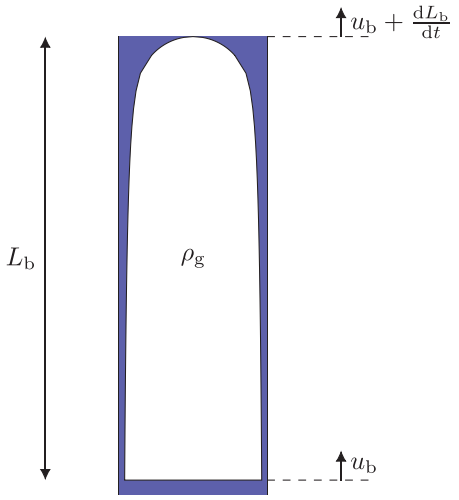

Fig. 8. Control Volume 2.

in fact, remained almost static along the complete simulation. As a consequence, downward liquid flow rate in the layer between bubble and duct wall is assumed constant and has a value of $U_\infty \pi \frac{D^2}{4}$. In what follows, we examine three control volumes.

The first control volume contains the liquid column above the bubble nose (see Figs. 6 and 7). Control volume upper boundary is determined by the free surface and has a velocity $u_{\mathrm{fs}}\mathbf{k}$, whereas lower boundary velocity is $\left(u_{\mathrm{b}} + \frac{\mathrm{d}L_{\mathrm{b}}}{\mathrm{d}t}\right)\mathbf{k}$. Velocity of liquid inside control volume 1 is assumed constant with value $u_{\mathrm{fs}}\mathbf{k}$. Here, $\mathbf{k}$ is the vertical unit vector and u_{b} is the velocity of the bubble bottom.

Mass conservation equation gives

$$\frac{\mathrm{d}L_{\mathrm{lc}}}{\mathrm{d}t} = u_{\mathrm{fs}} - u_{\mathrm{b}} - \frac{\mathrm{d}L_{\mathrm{b}}}{\mathrm{d}t}\,, \tag{19}$$

where L_{lc} is the liquid column height. Momentum conservation along vertical axis includes gravity, pressure and wall friction as external forces,

$$\frac{\mathrm{d}}{\mathrm{d}t}\left(\rho_{\mathrm{l}} L_{\mathrm{lc}} \frac{\pi D^2}{4} u_{\mathrm{fs}}\right) + \rho_{\mathrm{l}} \frac{\pi D^2}{4}\left[u_{\mathrm{fs}}(u_{\mathrm{fs}} - u_{\mathrm{fs}}) - u_{\mathrm{fs}}\left(u_{\mathrm{fs}} - u_{\mathrm{b}} - \frac{\mathrm{d}L_{\mathrm{b}}}{\mathrm{d}t}\right)\right] = - \rho_{\mathrm{l}} L_{\mathrm{lc}} \frac{\pi D^2}{4}|g| + P_0 \frac{\pi D^2}{4} - \frac{f}{8} L_{\mathrm{lc}} \pi D \rho_{\mathrm{l}} u_{\mathrm{fs}} |u_{\mathrm{fs}}|\,. \tag{20}$$

Insertion of Eq. (19) into Eq. (20) results in

$$\frac{P_0}{\rho_{\mathrm{l}}} = L_{\mathrm{lc}}\left[\frac{\mathrm{d}u_{\mathrm{fs}}}{\mathrm{d}t} + |g| + \frac{f}{2}\frac{u_{\mathrm{fs}}|u_{\mathrm{fs}}|}{D}\right], \tag{21}$$

where P_0 is the relative pressure at bubble nose and f is the friction factor.

The second control volume includes the bubble and its surrounding liquid (Fig. 8). The upper boundary velocity is $\left(u_{\mathrm{b}} + \frac{\mathrm{d}L_{\mathrm{b}}}{\mathrm{d}t}\right)\mathbf{k}$ and lower boundary velocity is $u_{\mathrm{b}}\mathbf{k}$. The liquid velocity on the upper boundary is $u_{\mathrm{fs}}\mathbf{k}$, while on the lower boundary (at $z = L_{\mathrm{b}}$) liquid velocity u can be calculated from the flow rate between bubble and duct wall,

$$U_\infty \pi \frac{D^2}{4} = \left(-u|_{z=L_{\mathrm{b}}} + U_\infty\right)[\pi \delta^*(D - \delta^*)]\,, \tag{22}$$

where $\delta^* = D/2 - r|_{z=L_b}$. Then, the mass conservation law for this control volume is,

$$\frac{d}{dt}(\rho_g V_g + \rho_l V_l) + \rho_l \pi \frac{D^2}{4}\left(u_{fs} - u_b - \frac{dL_b}{dt}\right) - \rho_l[\pi\delta^*(D-\delta^*)]\left(u|_{z=L_b} - u_b\right) = 0\,. \tag{23}$$

Now, by inserting Eq. (22) into mass conservation (Eq. (23)), and taking into account that the mass of gas is constant, mass conservation law can be written as

$$\frac{dV_l}{dt} = -\pi\frac{D^2}{4}\left(u_{fs} - u_b - \frac{dL_b}{dt}\right) - u_b\pi\delta^*(D-\delta^*) - U_\infty\left[\pi\frac{D^2}{4} - \pi\delta^*(D-\delta^*)\right]. \tag{24}$$

Moreover,

$$\frac{dV_l}{dt} = \frac{d}{dt}\left(\pi\frac{D^2}{4}L_b - V_g\right) = \frac{dV_g}{dt}(\psi - 1)\,, \tag{25}$$

$$\psi = \pi\frac{D^2}{4}\frac{dL_b}{dV_g} = \begin{cases} \left(1 - \frac{k\sqrt{gD}}{\sqrt{2gL_b}}\right)^{-1} & \text{if} \quad z_1 < L_b < z_2 \\ \frac{D^2}{4\left(\frac{D}{2}-\delta\right)^2} & \text{if} \quad L_b \geq z_2 \end{cases}, \tag{26}$$

where ψ comes from Eq. (17). Gas mass ($M_g = V_g\rho_g$) conservation combined with the compressibility model (18) leads to

$$\frac{dV_g}{dt} = -\frac{V_g}{\rho_g}\frac{d\rho_g}{dt} = -\frac{V_g}{\rho_g}\frac{1}{\gamma C}\left(\frac{P_0 + P_{atm}}{C}\right)^{1/\gamma - 1}\frac{dP_0}{dt}\,. \tag{27}$$

Gas pressure $P_0(t)$ is considered constant over the gas volume, as stated for bubble shape definition. To derive an explicit equation to compute u_{fs}, we introduce Eqs. (25), (26) and (27) into Eq. (24), resulting in

$$u_{fs} = (u_b - U_\infty)\left(1 - \frac{\delta^*(D-\delta^*)}{D^2/4}\right) - \frac{4}{\pi D^2}\frac{V_g}{\rho_g}\frac{1}{\gamma C}\left(\frac{P_0 + P_{atm}}{C}\right)^{1/\gamma - 1}\frac{dP_0}{dt}\,. \tag{28}$$

The third control volume consists of the gas bubble. To simplify the analysis, we employ as average bubble velocity the value of u_b. Thus, considering conclusions reported in Ref. [34], we can assume that gas velocity variations ascribed to gas expansion/compression are confined to a small region in the vicinity of the bubble nose; consequently, bubble momentum conservation equation is written as

$$\frac{d}{dt}[u_b(V_g\rho_g + K_M V_g\rho_l)] = |g|\rho_l V_g - \rho_l C_D\pi\frac{D^2}{4}\frac{u_b|u_b|}{2}, \tag{29}$$

where K_M and C_D are the added mass and drag coefficients, respectively. Added mass coefficient $K_M = \frac{\alpha\pi D^2 L_b}{4V_g}$, where α=0.32731 [35], and drag coefficient $C_D = \varepsilon\frac{V_g}{\pi(D/2)^3}$ [36]. Value of $\varepsilon \approx 8.4$ corresponds to a non-dimensional bubble velocity in stagnant liquid k=0.345 (Eq. (12)). Now, introduction of Eqs. (25), (26) and (27), attained in the second volume analysis, into Eq. (29) leads to

$$\beta\frac{du_b}{dt} = u_b\alpha\rho_l\psi\frac{V_g}{\rho_g}\frac{1}{\gamma C}\left(\frac{P_0 + P_{atm}}{C}\right)^{1/\gamma - 1}\frac{dP_0}{dt} + |g|\rho_l V_g - \rho_l\varepsilon V_g\frac{u_b|u_b|}{D}\,, \tag{30}$$

$$\beta = V_g\rho_g + \alpha\pi\frac{D^2}{4}L_b\rho_l\,.$$

Unknowns P_0, u_b, and u_{fs} can be computed by solving Eqs. (21), (28) and (30). Appendix B reports the simplified iterative solution procedure.

4.3.1. Discussion

In the vertical momentum law (21) we can consider that $|g| \gg \frac{u_{fs}}{dt}$ and $|g| \gg \frac{f}{2}\frac{u_{fs}|u_{fs}|}{D}$. These assumptions can be verified by solving the system of equations (21), (28) and (30), and comparing the aforementioned terms with gravity acceleration. Then, the bubble nose pressure is approximated as

$$P_0 = \rho_l L_{lc}|g|\,, \tag{31}$$

while, taking into account Eq. (19), pressure time derivative is

$$\frac{dP_0}{dt} = \rho_l|g|\left(u_{fs} - u_b - \frac{dL_b}{dt}\right). \tag{32}$$

Moreover, the first term on the right hand side of Eq. (30) is negligible respect to remaining forces (this observation is substantiated by extensive experiments for analytical solution (see section 4.4); accordingly, for (nearly) steady state conditions: $du_b/dt \to 0$, $u_b \to U_\infty$. Based on this premise, Eq. (28) reduces to

$$u_{fs} = -\frac{4}{\pi D^2}\frac{V_g}{\rho_g}\frac{1}{\gamma C}\left(\frac{P_0 + P_{atm}}{C}\right)^{1/\gamma - 1}\frac{dP_0}{dt}\,. \tag{33}$$

Finally, inserting Eq. (33) into Eq. (32),

$$\frac{dP_0}{dt} = \frac{-u_b}{\frac{1}{\rho_l|g|} - \frac{4(\psi-1)}{\pi D^2}\frac{V_g}{\rho_g}\frac{1}{\gamma C}\left(\frac{P_0 + P_{atm}}{C}\right)^{1/\gamma - 1}}\,. \tag{34}$$

Equation (34) reveals the condition for a sudden bubble expansion and, consequently, for a significant free surface vertical acceleration. The condition is

$$\rho|g|\frac{4(\psi-1)}{\pi D^2}\frac{V_g}{\rho_g}\frac{1}{\gamma C}\left(\frac{P_0 + P_{atm}}{C}\right)^{1/\gamma - 1} \to 1\,. \tag{35}$$

Next we study the stage when free surface has reached the upper end of the duct; in this situation liquid column height only depends on bubble dynamics and Eq. (19) reduces to,

$$\frac{dL_{lc}}{dt} = -u_b - \frac{dL_b}{dt}\,. \tag{36}$$

Following the same procedure as above, the time derivative of the bubble nose pressure is

$$\frac{dP_0}{dt} = \frac{-u_b}{\frac{1}{\rho_l|g|} - \frac{4\psi}{\pi D^2}\frac{V_g}{\rho_g}\frac{1}{\gamma C}\left(\frac{P_0 + P_{atm}}{C}\right)^{1/\gamma - 1}}\,, \tag{37}$$

and condition for a sudden expansion is

$$\rho_l|g|\frac{4\psi}{\pi D^2}\frac{V_g}{\rho_g}\frac{1}{\gamma C}\left(\frac{P_0 + P_{atm}}{C}\right)^{1/\gamma - 1} \to 1\,. \tag{38}$$

The determining variable in Eqs. (35) and (38) is the relation between gas volume V_g and the square of duct diameter D. The remaining parameters are constant or only suffer slight changes. From Eq. (26), $\psi > 1$, and in case of elongated bubbles, $\psi = \mathcal{O}(1)$. Hence when free surface reaches the upper conduit end, a considerably smaller gas volume is needed to provoke a sudden bubble expansion. Furthermore, once the bubble nose arrives at upper end, V_g rises to its maximum value, because compression originated from liquid column above the bubble has virtually vanished. In situ observations as well as numerical experiments (see [14] and references therein) provide evidences supporting that in this state a violent geyser may occur. Hypotheses assumed at the beginning of this section remain valid up to the state when bubble suffers a sudden expansion and liquid column is violently propelled. However conditions (35) and (38) can be used to foresee this dangerous situation, as will be pointed out in next section.

4.4. Assessment of Analytical Model

To validate the semi-analytical model we reproduce two experiments reported in Ref. [22]. Experiments consist of a vertical tube of length L_d=0.610 m, having the top open to the atmosphere. The tube is connected below to a horizontal duct with a diameter of 0.094 m. The vertical duct has a diameter D=0.057 m (experiment 1) or D=0.0127 m (experiment 2). An air mass M_g=4.642·10^{-3} kg introduced into the horizontal duct propagates towards vertical tube base (see sketch in Fig. 9), and climbs up the vertical duct. Eventually, the air mass causes geysering at the top of vertical tube. For the semi-analytical model we assume that the vertical tube has semi-infinite length, with origin in the open upper end situated at H=0.610 m (see vertical conduit in Fig. 9). Water density ρ_l=1000 kg/m^3, gas reference density ρ_{g0}=1.2 kg/m^3, and g=9.81 m/s^2. Initial condition is considered when air pocket has reached the vertical pipe base, thus h_b^0=0.0 m, h_{fs}^0=0.254 m, and initial air pressure value is 0.254 m of water column. Non-dimensional results of three laboratory test repetitions and of semi-analytical model are shown in Figs. 10 and 11 for experiments 1 and 2, respectively. Figures depict the history of bubble head position h_b (Figs. 10a and 11 a), free surface position h_{fs} (Figs. 10b and 11 b) and bubble pressure h_p (Figs. 10c and 11 c), where $\{h_b^*, h_{fs}^*, h_p^*\} = \{h_b, h_{fs}, h_p\}/L_d$, $h_p = P_0/(g\cdot\rho_l)$ and $t^* = t\sqrt{gD}/L_d$.

The model reproduces the quasi-constant bubble head celerity in test 1 (see Fig. 10a). Gas expands faster under conditions of test 2, and bubble head has an apparent vertical acceleration (Fig. 11a). For case 1, the value of the left hand side in sudden expansion condition (35) is 0.008. Instead, the value of left hand side for test 2 rises to 0.35. In both cases the analytical model results have a good agreement with laboratory measurements. Free surface position is well captured in test 2 (Fig. 11b) and slightly underpredicted in test 1 (Fig. 10b), while oscillatory free surface behaviour shown in laboratory is

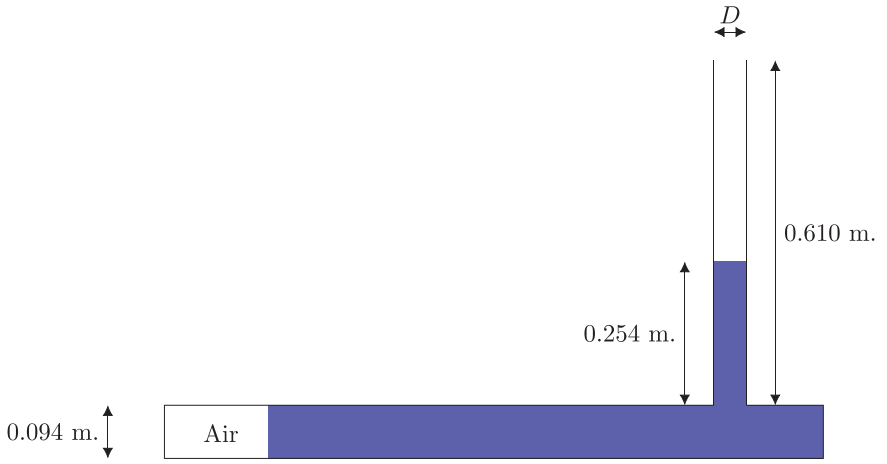

Fig. 9. Sketch for semi-analytical model assessment.

adequately reproduced. Reader can detect a (nearly) vanishing of oscillations in test 2, both in lab and model. This absence of oscillations usually evinces that conditions (35) or (38) are close to being fulfilled and, therefore, a stage much closer to the formation of a high velocity vertical jet. Finally, analytical bubble pressure shows a good agreement with the three laboratory series in both tests (see Figs. 10c and 11 c); in particular, amplitude and period of pressure oscillations in test 1 are very similar to laboratory observations. The model introduced in Ref. [22] also reproduces bubble and free surface positions fairly well; nonetheless, bubble pressure is more precisely replicated by the present model. Analytical results show that bottom bubble velocity remains quasi-constant in time for both experiments, having a value $u_b \approx U_\infty$, and proves that assumptions of Eq. (30) are valid.

4.5. Approach to Multiple Bubbles

Here we consider N bubbles rising in a vertical duct (Fig. 12), where L_{bj} is the length of bubble j and L_{lcj} is the length of the liquid column above bubble j. Bubble numbering starts from the lowest one, so the nearest to the free surface is bubble N. Liquid columns between bubbles are long enough such that trailing bubble is not affected by the leading one. Thus following Ref. [37], $L_{lcj} > 10D$, for $1 \le j < N$.

Each bubble pushes the above liquid column, including leading one, with mean velocity u_{fsj}. Hence bubble j velocity is

$$u_{bj} = u^*_{bj} + C_I \cdot \sum_{i=1}^{j-1} u_{fsi}\,, \tag{39}$$

where u^*_{bj} is the bubble relative velocity respect to surrounding liquid, and parameter C_I takes into account deviation of maximum velocity from mean velocity in the profile ahead bubble $j-1$. An approximate value of C_I is 1.2 for turbulent flows and 2.0 for laminar flows [29]. Velocity u_{fsj} is calculated in a similar way as velocity calculated by Eq. (28),

$$u_{fsj} = \left(u^*_{bj} + (C_I - 1)\sum_{i=1}^{j-1} u_{fsi} - U_\infty\right)\left(1 - \frac{\delta^*_j\left(D - \delta^*_j\right)}{D^2/4}\right) - \frac{4}{\pi D^2}\frac{V_{gj}}{\rho_{gj}}\frac{1}{\gamma C}\left(\frac{P_{0j} + Patm}{C}\right)^{1/\gamma - 1}\frac{dP_{0j}}{dt}\,, \quad \text{for } 1 < j \le N\,, \tag{40}$$

$$u_{fs1} = \left(u^*_{b1} - U_\infty\right)\left(1 - \frac{\delta^*_1\left(D - \delta^*_1\right)}{D^2/4}\right) - \frac{4}{\pi D^2}\frac{V_{g1}}{\rho_{g1}}\frac{1}{\gamma C}\left(\frac{P_{01} + Patm}{C}\right)^{1/\gamma - 1}\frac{dP_{01}}{dt}\,. \tag{41}$$

Likewise, equation for u^*_{bj} resembles calculation of u_b in Eq. (30),

$$\beta_j \frac{du^*_{bj}}{dt} = u^*_{bj}\alpha\rho_l\psi_j\frac{V_{gj}}{\rho_{gj}}\frac{1}{\gamma C}\left(\frac{P_{0j} + Patm}{C}\right)^{1/\gamma - 1}\frac{dP_{0j}}{dt} + |g|\rho_l V_{gj} - \rho_l \varepsilon V_{gj}\frac{u^*_{bj}\left|u^*_{bj}\right|}{D}\,, \tag{42}$$

$$\beta_j = V_{gj}\rho_{gj} + \alpha\pi\frac{D^2}{4}L_{bj}\rho_l\,.$$

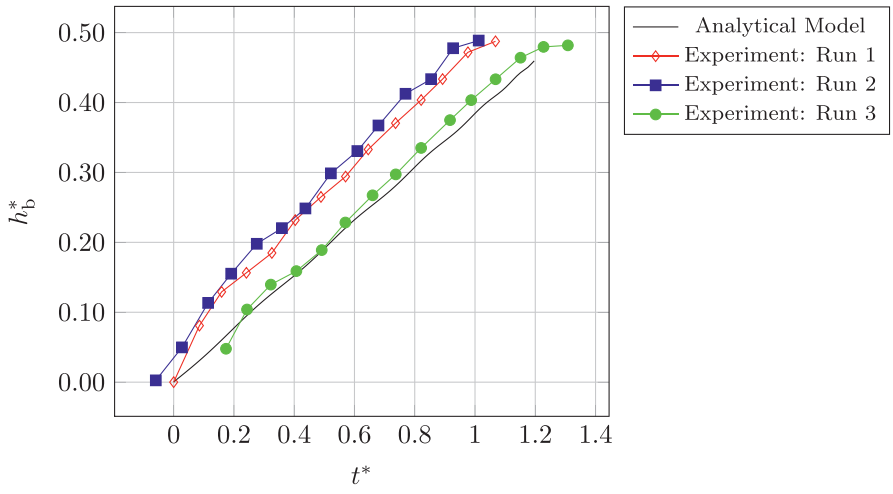

(a) Bubble position

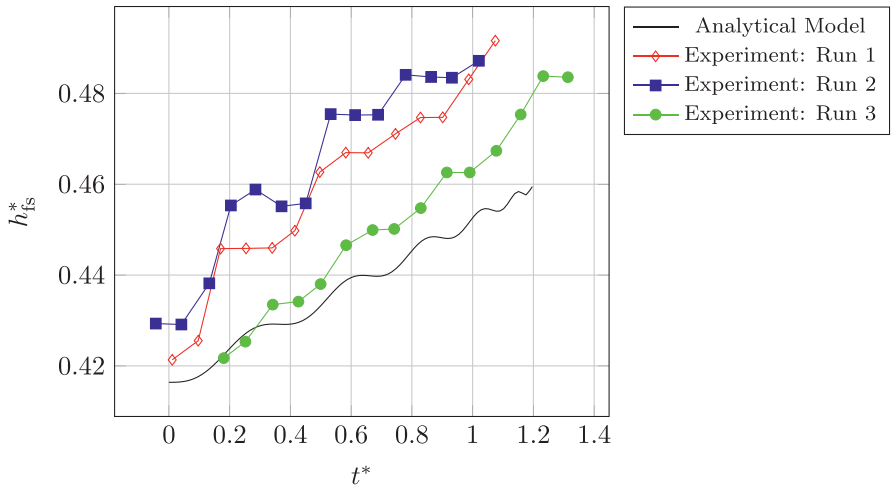

(b) Free surface position

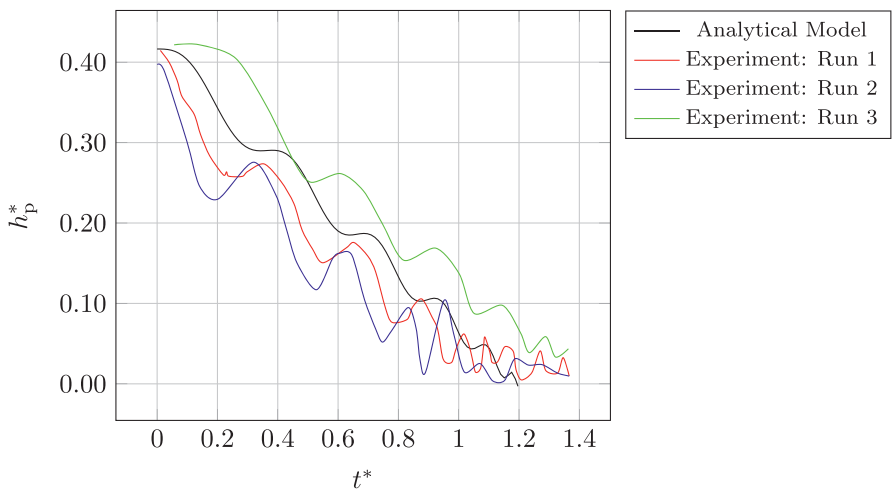

(c) Bubble pressure

Fig. 10. Rising bubble, test 1: $D = 5.700 \cdot 10^{-2}$ m. Comparison between semi-analytical model and experimental results [22].

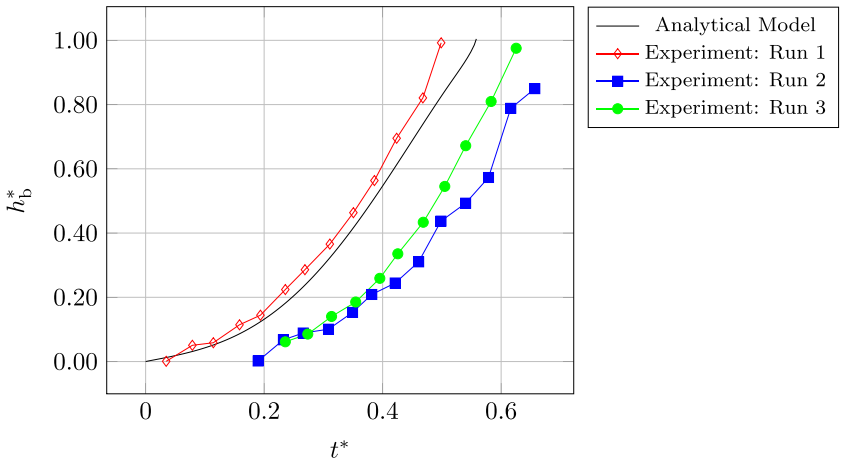

(a) Bubble position

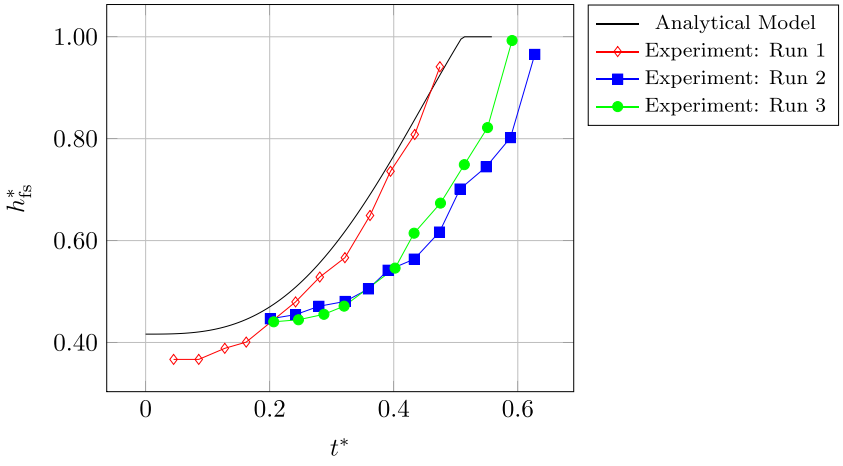

(b) Free surface position

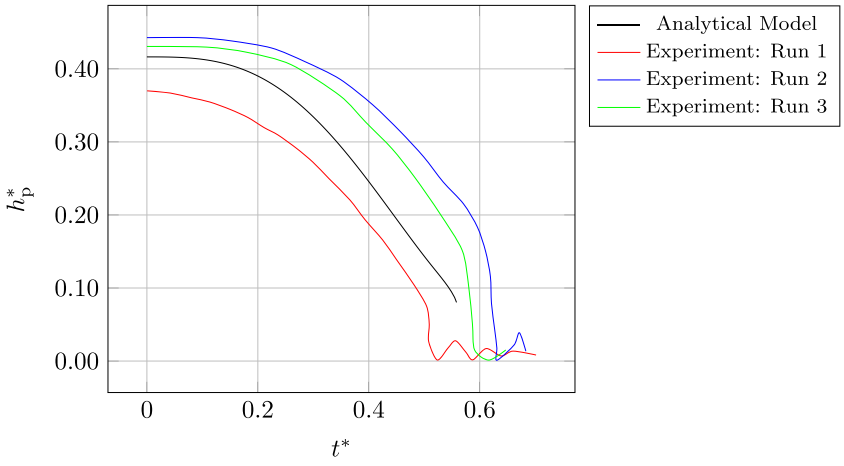

(c) Bubble pressure

Fig. 11. Rising bubble, test 2: $D = 1.269 \cdot 10^{-2}$ m. Comparison between semi-analytical model and experimental results [22].

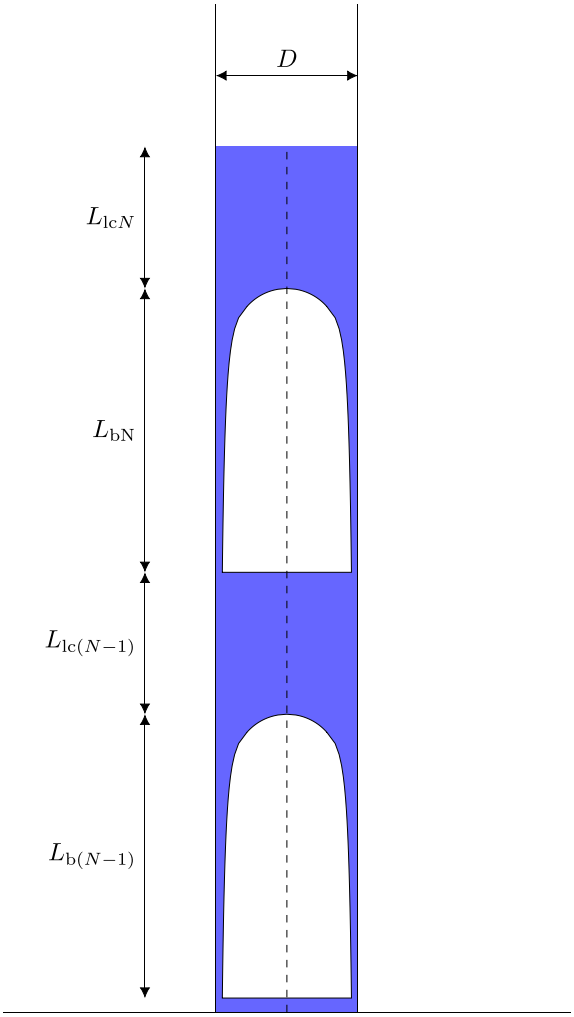

(a) Top

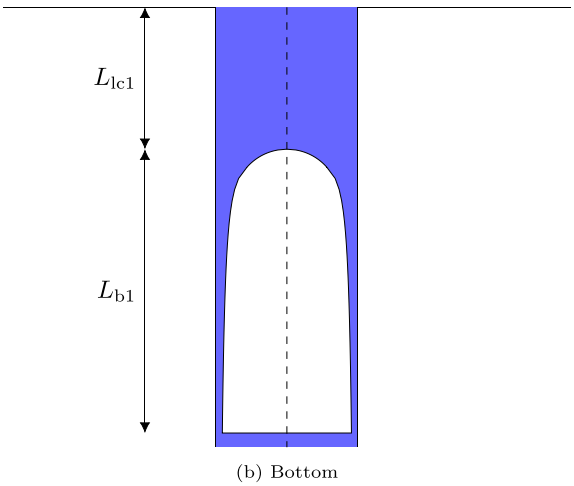

(b) Bottom

Fig. 12. Sketch of multiple bubbles.

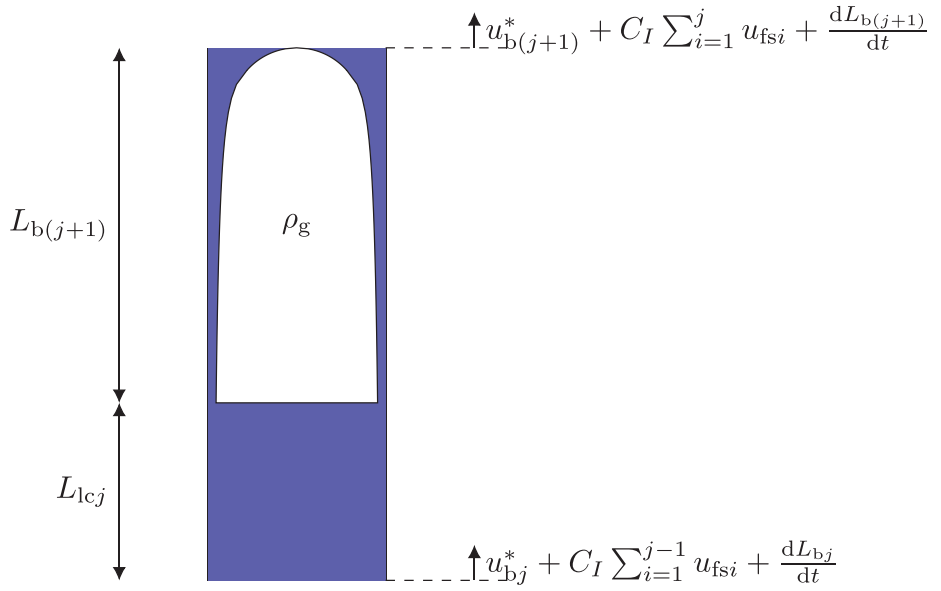

Fig. 13. Control Volume 3.

To close the system, we add equations for $\frac{\mathrm{d}L_{\mathrm{lc}j}}{\mathrm{d}t}$, $\frac{\mathrm{d}L_{\mathrm{b}j}}{\mathrm{d}t}$, and for the relative pressure P_{0j} at bubble j nose. For that purpose, we study a control volume including bubble $j+1$ and liquid column j (Fig. 13).

Lower and upper boundaries move according to the nose of bubble j and $j+1$, respectively. Thus, liquid average velocity at lower boundary is $\sum_{i=1}^{j} u_{\mathrm{fs}i}\mathbf{k}$, while at upper boundary is $\sum_{i=1}^{j+1} u_{\mathrm{fs}i}\mathbf{k}$. Mass conservation in the control volume results in

$$\frac{\mathrm{d}L_{\mathrm{lc}j}}{\mathrm{d}t} = -u_{\mathrm{fs}(j+1)} + u^*_{\mathrm{b}(j+1)} + C_I u_{\mathrm{fs}j} - u^*_{\mathrm{b}j} - \frac{\mathrm{d}L_{\mathrm{b}j}}{\mathrm{d}t} + \frac{4}{\pi D^2}\frac{\mathrm{d}V_{\mathrm{g}(j+1)}}{\mathrm{d}t}, \quad \text{for } 1 \le j < N, \tag{43}$$

$$\frac{\mathrm{d}L_{\mathrm{lc}N}}{\mathrm{d}t} = u_{\mathrm{fs}N} - u^*_{\mathrm{b}N} - \frac{\mathrm{d}L_{\mathrm{b}N}}{\mathrm{d}t} - (C_I - 1)\sum_{i=1}^{N-1} u_{\mathrm{fs}i}, \tag{44}$$

and, if water reaches the top end of the duct,

$$\frac{\mathrm{d}L_{\mathrm{lc}N}}{\mathrm{d}t} = -u^*_{\mathrm{b}N} - \frac{\mathrm{d}L_{\mathrm{b}N}}{\mathrm{d}t} - C_I \sum_{i=1}^{N-1} u_{\mathrm{fs}i}. \tag{45}$$

To apply momentum conservation we assume that liquid moves with velocity $\sum_{i=1}^{j} u_{\mathrm{fs}i}\mathbf{k}$, neglecting local bubble effects as well as gas momentum, given that normally $\frac{\rho_{\mathrm{g}}}{\rho_{\mathrm{l}}} \ll 1$. Thus, momentum conservation equation along vertical axis yields to

$$\frac{P_{0j}}{\rho_{\mathrm{l}}} = \frac{P_{0(j+1)}}{\rho_{\mathrm{l}}} + \left[L_{\mathrm{b}(j+1)} + L_{\mathrm{lc}j} - \frac{4V_{\mathrm{g}(j+1)}}{\pi D^2}\right]\left(\frac{\mathrm{d}}{\mathrm{d}t}\left(\sum_{i=1}^{j} u_{\mathrm{fs}i}\right) + |g|\right) \tag{46}$$

$$+ u_{\mathrm{fs}(j+1)}\left(u_{\mathrm{fs}(j+1)} - u^*_{\mathrm{b}(j+1)} - (C_I - 1)\sum_{i=1}^{j} u_{\mathrm{fs}i} - \frac{\mathrm{d}L_{\mathrm{b}(j+1)}}{\mathrm{d}t}\right) \tag{46}$$

$$+ \frac{f}{2D}\left(\sum_{i=1}^{j} u_{\mathrm{fs}i}\left|\sum_{i=1}^{j} u_{\mathrm{fs}i}\right|\right)\left(L_{\mathrm{b}(j+1)} + L_{\mathrm{lc}j}\right), \quad \text{for } 1 \le j < N, \tag{46}$$

$$\frac{P_{0N}}{\rho_{\mathrm{l}}} = L_{\mathrm{lc}N}\left[\frac{\mathrm{d}}{\mathrm{d}t}\left(\sum_{i=1}^{N} u_{\mathrm{fs}i}\right) + |g| + \frac{f}{2D}\left(\sum_{i=1}^{N} u_{\mathrm{fs}i}\left|\sum_{i=1}^{N} u_{\mathrm{fs}i}\right|\right)\right]. \tag{47}$$

Time variation of bubble length and volume are

$$\frac{\mathrm{d}L_{\mathrm{b}j}}{\mathrm{d}t} = \frac{4\psi_j}{\pi D^2}\frac{\mathrm{d}V_{\mathrm{g}j}}{\mathrm{d}t},$$

$$\frac{dV_{gj}}{dt} = -\frac{V_{gj}}{\rho_{gj}}\frac{1}{\gamma C}\left(\frac{P_{0j}+Patm}{C}\right)^{1/\gamma-1}\frac{dP_{0j}}{dt}.$$

Although solution algorithm is analogous to one single bubble algorithm (Appendix B), the new situation has $3N$ equations (Eqs. (40), (41), (42), (46) and (47)) for the $3N$ unknowns. Equations (43) and (44) (or Eq. (45) if the free surface reaches the top end of the duct) update the length of the liquid columns.

4.6. Discussion and Assessment

By following analogous assumptions to those discussed for one bubble dynamics in subsection 4.3.1, if $u^*_{bj} = U_\infty$ and C_l=1, eqs. (40) and (44) for bubble N reduce to

$$u_{fsN} = -\frac{4}{\pi D^2}\frac{V_{gN}}{\rho_{gN}}\frac{1}{\gamma C}\left(\frac{P_{0N}+Patm}{C}\right)^{1/\gamma-1}\frac{dP_{0N}}{dt} \tag{48}$$

and

$$\frac{dL_{lcN}}{dt} = u_{fsN} - U_\infty - \frac{dL_{bN}}{dt}, \tag{49}$$

respectively. Furthermore, $|g| \gg \frac{\partial}{\partial t}\sum_{i=1}^{N} u_{fsi} + \frac{f}{2D}\sum_{i=1}^{N} u_{fsi}\left|\sum_{i=1}^{N} u_{fsi}\right|$ and Eq. (47) for bubble N results in

$$\frac{P_{0N}}{\rho_l} = L_{lcN}|g|. \tag{50}$$

Thus occurrence of sudden expansion for top bubble has similar conditions to those for a single bubble (see Eqs. (31)–(33)). Besides, abrupt expansion also have an effect on the remaining air pockets (see Eq. (46)).

We replicate second test of section 4.4, and consider in this case two consecutive bubbles with $L_{lc1} = L_{lc2}$=0.254 m (lengths of the liquid column above bubble 1 and 2, respectively). To elucidate the influence of the lower bubble dynamics on the top bubble dynamics we solve the non-abridged equations (40), (41), (42), (46) and (47) with C_l=1.2. Computations are performed for three setups: a single bubble with M_g=4.642·10^{-3} kg, a single bubble with double mass M_g=9.284·10^{-3} kg, and two bubbles with $M_{g1} = M_{g2}$=4.642·10^{-3} kg. Fig. 14 depicts analytical results of the three setups for top bubble position (Fig. 14a), free surface position (Fig. 14b), and top bubble pressure (Fig. 14c). The figures reveal a slightly higher upper bubble velocity and free surface velocity in comparison with a single bubble; these increases are nonetheless lower than in the case of joined bubbles. In real cases, detachments among the three setups can be less significant as the semi-analytical solution moderately overpredicts velocities in the third configuration. This is because the model adopts the same pressure for all gas contained in each bubble, which may amplify expansion action for very large bubbles since we do not consider that those bubble regions far from the nose may have higher pressures.

The last test for the semi-analytical model is the development of geysering caused by multiple bubbles. From experimental and in situ observations, when a train of air pockets rises in a vertical pipe, the first bubble seems to produce the weakest geyser, measured in terms of height and average velocity of the jet [38]. A reason for this can be the loss of liquid during the first geyser expelling, which involves a sudden decrease of pressure in the remaining bubbles. In this test we intend to qualitatively reproduce laboratory observations of Ref. [38] with the semi-analytical model. Now vertical duct has D=0.152 m, total volume of the two air pockets at atmospheric pressure is 1.7 m^3, L_{lc1}=4 m, and L_{lc2}=6 m. In lab experiments, first bubble appears to be smaller than remaining ones (see snapshots in Fig. 7 of Ref. [38]). To recreate this observation we set M_{g1}=1.68 kg and M_{g2}=0.36 kg. At the initial time, the free surface is located at the top end of the duct. Once the nose of bubble 2 reaches the free surface, the problem is solved by the system of equations for one single bubble with L_{lc} determined by

$$L_{lc} = L_{lc1}^{(n-1)} + \omega\left(L_{b2}^{(n-1)} - \frac{4V_{g2}^{(n-1)}}{\pi D^2}\right), \tag{51}$$

where super-index $(n-1)$ indicates time just before bubble 2 gets to the free surface, and parameter ω determines the percentage of liquid previously located between bubble 2 and duct wall remaining in the duct. We assume ω=0.5.

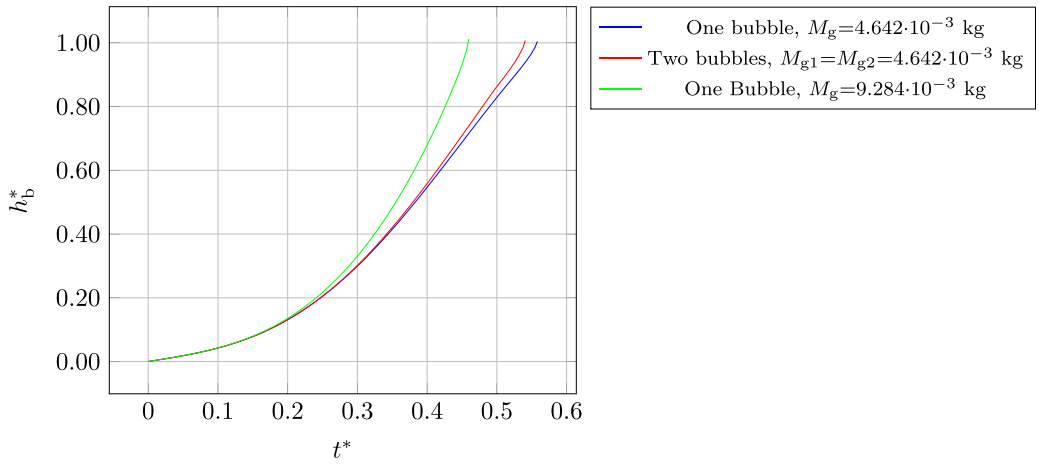

(a) Top bubble position

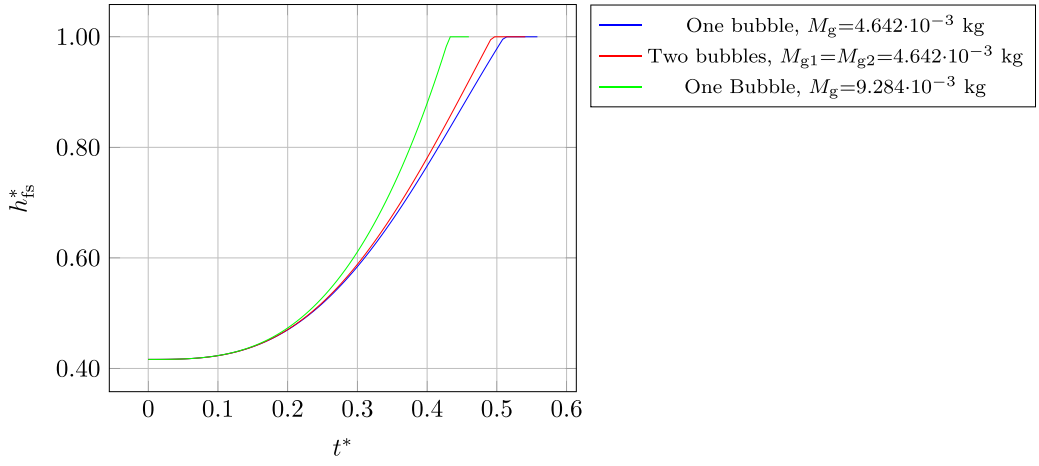

(b) Free surface position

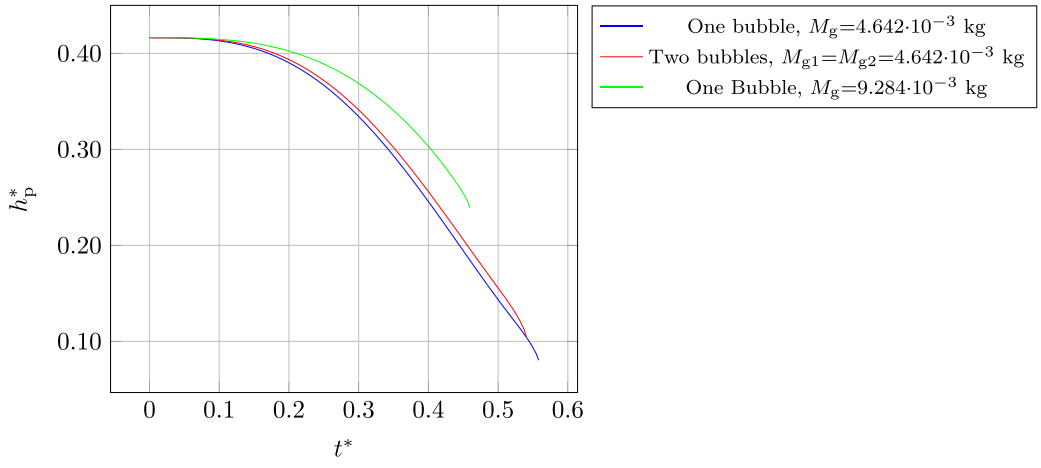

(c) Top bubble pressure

Fig. 14. Comparison between one single bubble with different gas masses and two consecutive bubbles.

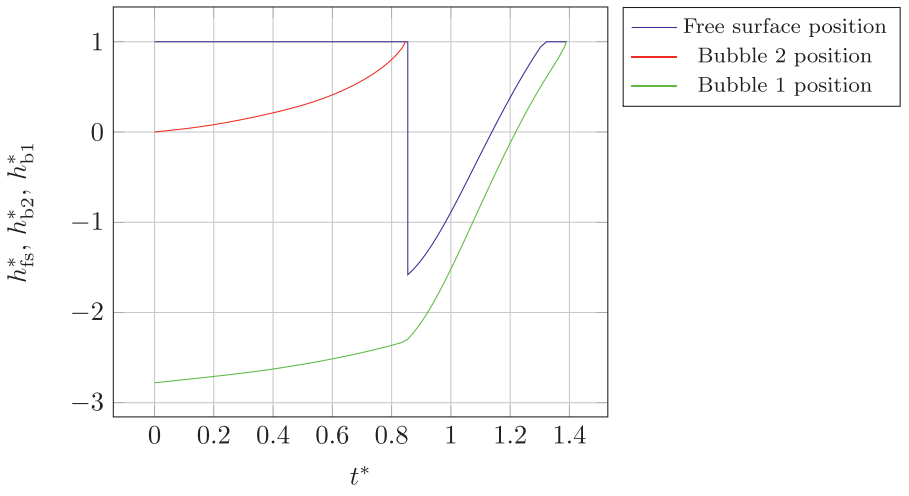

(a) Free surface and bubbles heights.

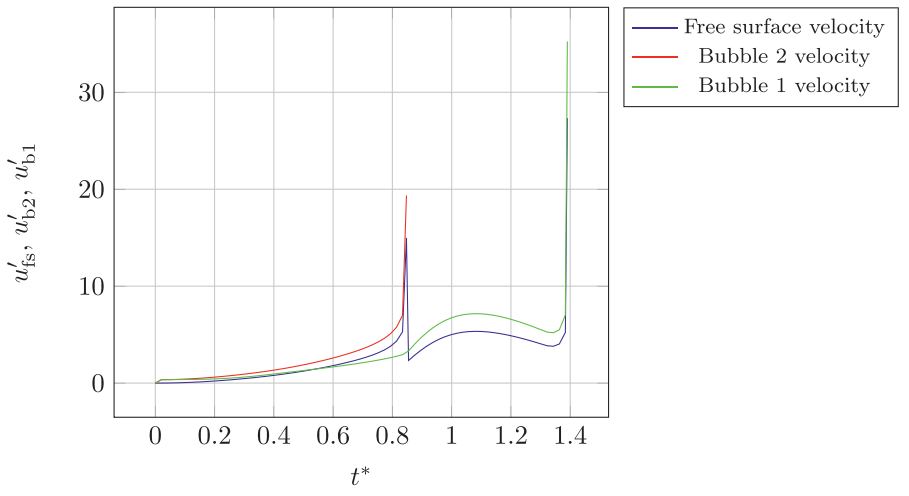

(b) Free surface and bubbles velocities

Fig. 15. Geysering event due to two consecutive bubbles.

The semi-analytical model is able to reproduce laboratory observations, despite the fact that the model does not consider the resulting diffuse air/water transition in the vertical duct when first bubble reaches the free surface. Fig. 15 shows non-dimensional analytical results for free surface and bubbles position (Fig. 15a) and velocities (Fig. 15b), where $\{h^*_{fs}, h^*_{b2}, h^*_{b1}\} = \{h_{fs}, h_{b2}, h_{b1}\}/L_{lc2}$, $\{u'_{fs}, u'_{b1}, u'_{b2}\} = \{u_{fs}, u_{b1}, u_{b2}\}/\sqrt{gD}$, $t^* = t\sqrt{gD}/L_{lc2}$, and u_{fs}, u_{bj} are the absolute velocities of free surface and bubble j nose, respectively.

When the leading bubble reaches the free surface at $t^* \approx 0.85$, the velocity of the trailing bubble increases as can be seen in Fig. 15b (green line). This increment depends to some extent on the bubble pressure change, which is mainly determined by the amount of water expelled during first geyser. Hence, smaller values of ω gives larger increases of trailing bubble velocity in analytical outputs. After first discharge, remaining water above trailing bubble is driven to the top end of the duct causing a second geyser. Strength of last eruption is greater than previous one as can be checked by comparing free surface velocity values at $t^* \approx 0.85$ and $t^* \approx 1.4$ in Fig. 15b. This state where second eruption is stronger than first one (also reported in Ref. [38]) is due to two reasons. First, relation between gas volume of trailing bubble and square of duct diameter is large enough; second, free surface arrives at the duct top end before trailing bubble nose reaches the free surface. In this way, sudden expansion of gas is more likely to happen as in test 2 of previous section (see Fig. 11). Conversely, if water column ahead the trailing bubble is too large or bubble gas mass is small, momentum transferred from air to water may

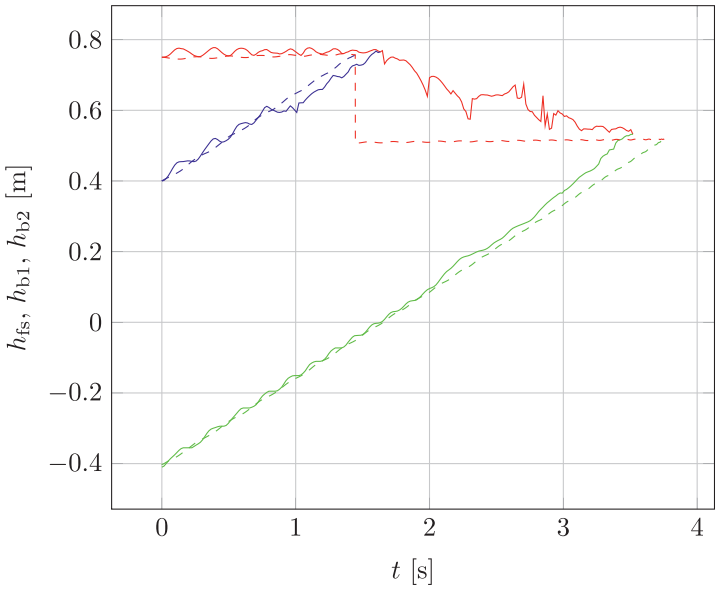

Fig. 16. Two bubbles rising in a vertical duct, analytical and numerical results for free surface and bubble positions as a function of time. Solid and dashed lines represent numerical and analytical results respectively. Red lines depict free surface position and blue and green lines show leading and trailing bubbles position respectively.

not be sufficient to propel violently the column of liquid. In this case, free surface position would oscillate as in test 1 of previous section (see Fig. 10).

5. Numerical Experiments

5.1. Two bubbles rising in a vertical duct

We compare the semi-analytical model with the numerical model for multiple bubbles dynamics. The experiment consists of a vertical duct of length L_{d}=2.0 m and diameter D=0.05 m filled with water up to z=0.75 m (origin of z coordinate is at half the height of the tube). Two air bubbles are inside the duct with their noses situated at z=0.4 m and at z=-0.41 m; both bubbles have a length L_{b}=0.305 m (Fig. 17a). At initial time fluids are at rest, and bubbles air pressure values are 0.35 m and 1.16 m of water column. The same initial conditions are applied for the two models. We use an axisymmetric version of the numerical model, whose formulation can be found in section 3.5.3 of Ref. [14]. This kind of simplified approach has demonstrated a good performance in previous studies involving rising bubbles (see e.g. Ref. [39]). Physical parameters values are the same as in section 3. Average element length of axisymmetric mesh is $\delta = 6.25\sqrt{2}\cdot 10^{-4}$ m, $\Delta t = 4\cdot 10^{-5}$ s, reinitialization parameters are $\varepsilon = 0.83\Delta l$, $\Delta\tau = 0.1\Delta l^2/(8\varepsilon)$, and parameter $\Upsilon = \Delta l/(6000\varepsilon)$. Slip condition is applied on all boundaries except on the upper one, where inlet/outlet condition is used to allow the air to inflow/outflow. Gas expansion is not as consequential as in the tests of section 4.6, nevertheless it is relevant to compare analytical and numerical to scrutinize constraints of the theoretical approach.

The histories of free surface position h_{fs} and bubbles nose positions h_{b1}, h_{b2} are plotted in Fig. 16, where analytical and numerical outputs are marked with dashed and solid lines, respectively. Free surface position is specified as the highest point on tube axis with $\phi > 0.5$, and each bubble nose position is specified as highest position with $\phi < 0.5$. Numerical results at different times are depicted in Figs. 17b–17 e. Free surface and bubbles head positions are well captured by the semi-analytical model for $t < 1.6$ s, although a slight over-prediction of upper bubble position is observed between t=0.8 s and t=1.6 s. This is probably due to detached secondary small bubbles (see Figs. 17b-17 c), only appraised by the numerical algorithm. This detachment reduces gas mass and bubble length, altering gas expansion effect and bubble velocity. Furthermore, the effect of emergence of downstream wakes during pocket rising is not considered in the analytical approach. Once the upper bubble reaches free surface, the analytical solution predicts a sudden decrease in free surface level because the entire gas mass is assumed to be released at the same time. Instead, numerical model can not capture free surface location precisely, because detached bubbles transform it into a diffuse air/water interface (see Figs. 16, 17 d and 17 e), seemingly, a more realistic event. Nonetheless both solutions tend to converge over time (see results in Fig. 16, e.g. at $t \approx 3.1$s). Lastly, numerical results show a slight acceleration of the trailing bubble from $t\approx$ 2 s, not foretold by semi-

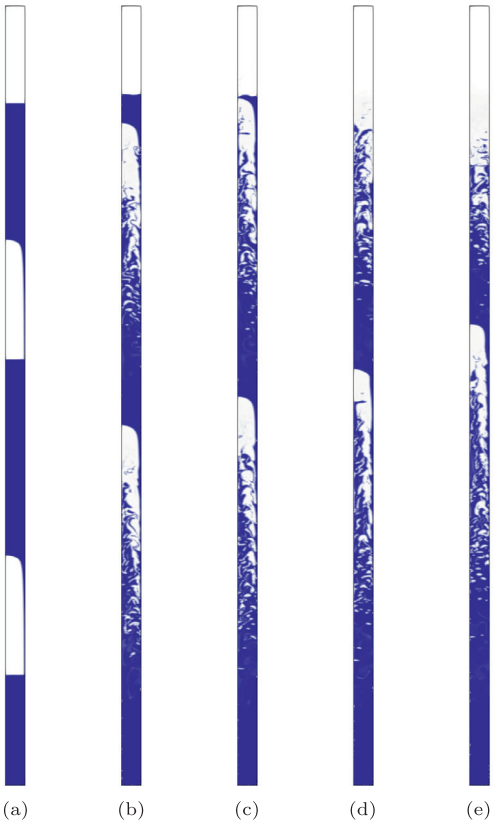

Fig. 17. Two bubbles rising in a vertical duct, numerical results at times (a)0.00s, (b)1.28s, (c)1.60s, (d)1.92s and (e)2.24s. Horizontal axis is scaled by 2.

analytical model. This behaviour is ascribed to the wake of the leading bubble, and was also observed in swarms of small bubbles [40].

5.2. Geysering Simulation

The last experiment is a full coupled three dimensional computation of a closed air cavity propagation, air and momentum transfer from nearly horizontal to vertical conduits, and geysering. An air bag is entrapped in an inclined duct connected to ground level by a saturated vertical shaft (Fig. 18). Main duct has a diameter of 1.5 m, a length of 17 m, and an inclination of 5° with respect to the horizontal. Vertical conduit has a diameter of 0.5 m, a length of 4.207 m, and joins the main duct at a distance of 5.0 m from main duct left end. The numerical domain has a $4 \times 4 \times 5$ m chamber with its base on ground level (see Fig. 18), to allow water to leave the domain and air to outflow/inflow. Fluids are assumed nearly-incompressible. Physical parameters are ρ_1=1.225 kg/m^3, $\mu_1 = 1.8 \cdot 10^{-5}$ kg/(ms), $a_1^2 = 10^5$ m^2/s^2 (air), ρ_2=1000 kg/m^3, $\mu_2 = 10^{-3}$ kg/(ms), $a_2^2 = 2.2 \cdot 10^6$ m^2/s^2 (water), σ=0.07 N/m and $|\mathbf{g}|$=9.81 m/s^2. Average element length[2] is $\delta_{3D} = 1.71 \cdot 10^{-2}$ m and $\Delta t = 2.0 \cdot 10^{-4}$ s. Reinitialization parameters are $\varepsilon = 0.67\Delta l$ and $\Delta\tau = 0.1\Delta l^2/(8\varepsilon)$, and $\Upsilon = \Delta l/(600\varepsilon)$. A slip boundary condition is applied on solid walls (black lines in Fig. 18). This condition is adequate in the simulation of air cavities and rising Taylor bubbles (see numerical experiments of previous sections and of Ref. [14]). An inlet/outlet condition is used on the chamber upper boundary (red line in Fig. 18). At initial time, the water level is situated at 0.1 m below ground level, and air occupies approximately the last 8 meters of the inclined duct. Initial air volume is about 14 m^3 and air pressure is 5.5 m of water column.

[2] Average element length for 3D unstructured meshes is $\delta_{3D} = \sqrt[3]{\frac{\sum_1^N V_i}{N}}$, where V_i is the volume of tetrahedron i and N is the total number of tetrahedrons.

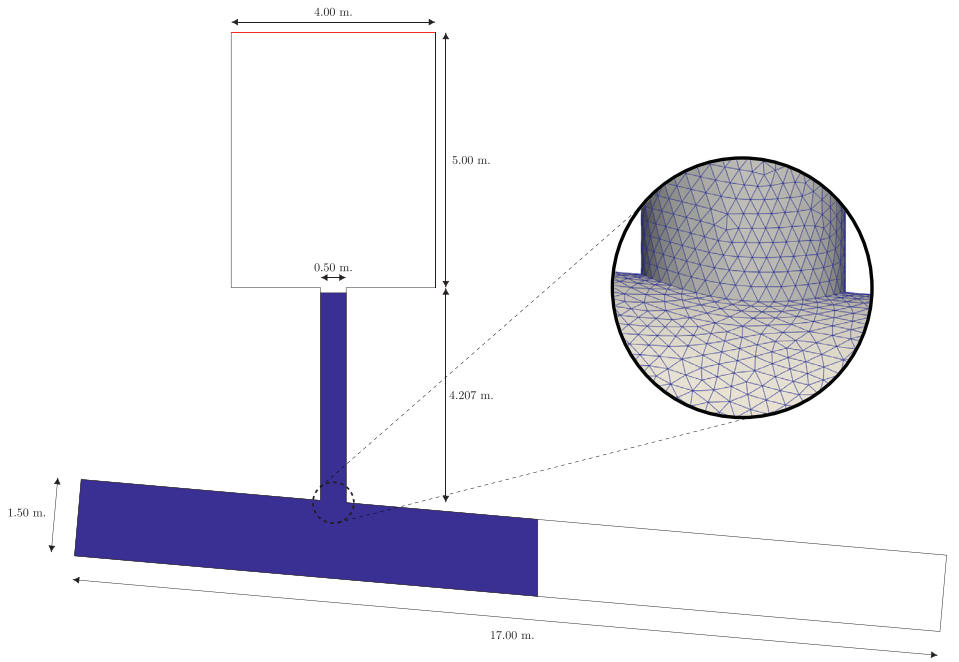

Fig. 18. Domain for geysering simulation and detail of the mesh. Black color boundary: Slip condition; red color boundary: inlet/outlet condition. Blue color indicates regions occupied by water at initial time step.

At the initial propagation stage, entrapped air expands because pressure is discontinuous across air/water interface; as a consequence, free surface in vertical shaft rises as can be seen in Fig. 5.2a. Bubble reaches the base of the vertical duct at $t \approx 1.63$s and starts to ascend. The bubble nose position is plotted in Fig. 22 superimposed on the analytical solution. Both solutions show the same trend. In the case of the numerical result, bubble velocity values are higher when the pocket starts to rise because of the extra momentum picked up during its propagation along the inclined duct; then this momentum is partially transferred to vertical component (e.g. at the state plot in Fig. 5.2b). Both numerical and analytical bubble velocities are much higher than U_∞=0.764 m/s (see section 4.1), because now gas expansion effects are significant.

As the air pocket travels along the vertical tube, the water free surface has a twofold shape. Along with the radial propagation of a shallow layer of water, a mushroom shape rises (Figs. 5.2b-5.2 d and Fig. 20a). This observation is in agreement with real geysering events (see first frame of Fig. 21) and experiments performed in Ref. [14]. The bubble reaches ground level at $t \approx 2.58$s, and then water is ejected upwards, resulting in a geyser that reaches a height of 4.0 m over the ground level (see sequence 5.2 e-5.2 g and Fig. 20b). Although mesh resolution is not enough to capture the waterspray expelled from the duct, the flow pattern (almost axisymmetric) is similar to real geyser events (compare Fig. 20b and the second frame of Fig. 21). Flow patterns found when air bubble reaches the ground level are also comparable to those obtained in other works involving air pockets breaking the free surface, as in Ref. [41], where the influence of bubble characteristics on the splashing in bath smelting plants was investigated. In that work, authors concluded that the amount of splashes, and the height reached by them, rise with the increase of gas flow rate and with the depth at which bubbles are produced, in line with findings presented in Section 4.

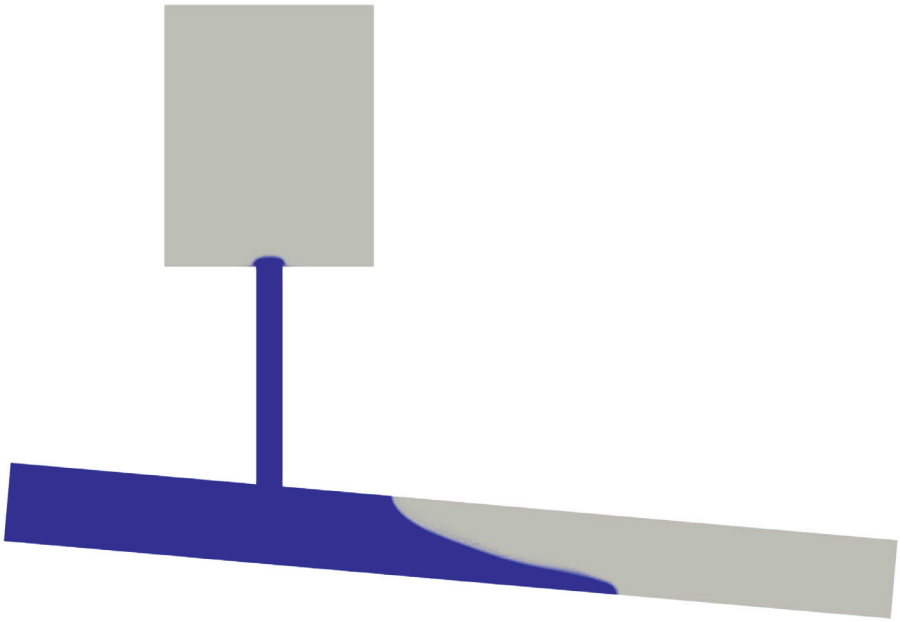

(a) t=0.75 s.

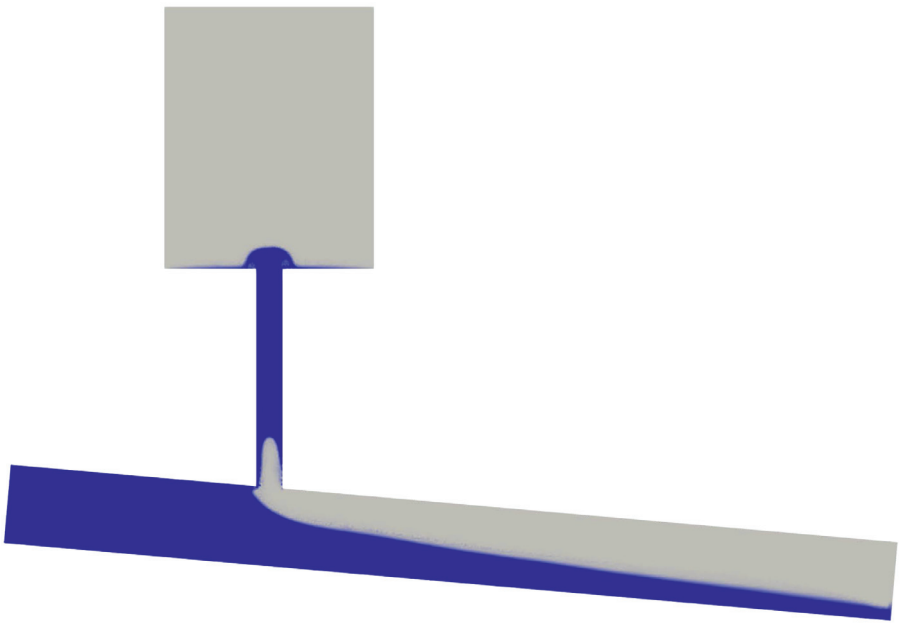

(b) t=2.00 s.

Fig. 19. Geysering experiment, phase function results.

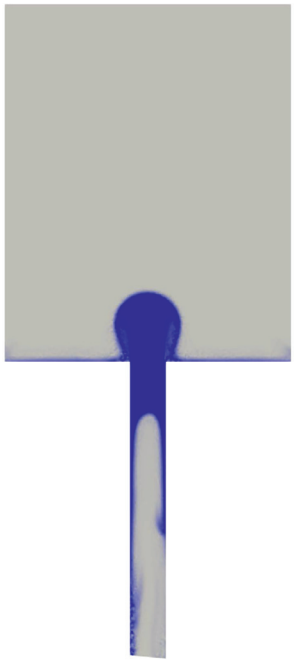

(c) t=2.50 s.

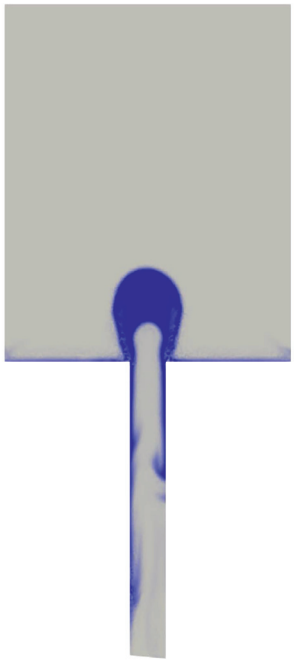

(d) t=2.625 s.

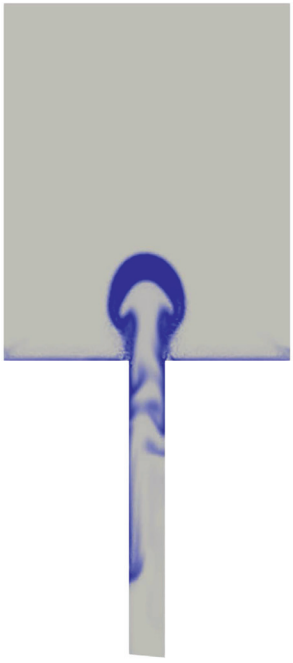

(e) t=2.675 s.

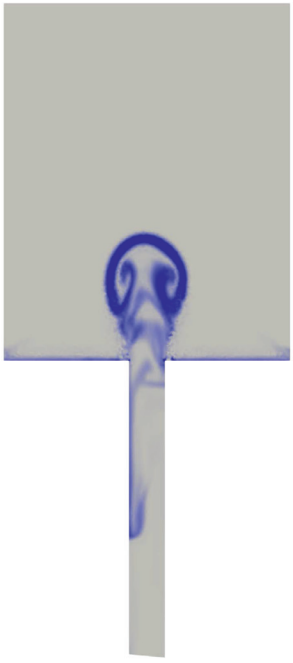

(f) t=2.725 s.

(g) t=2.850 s.

Fig. 19. Continued

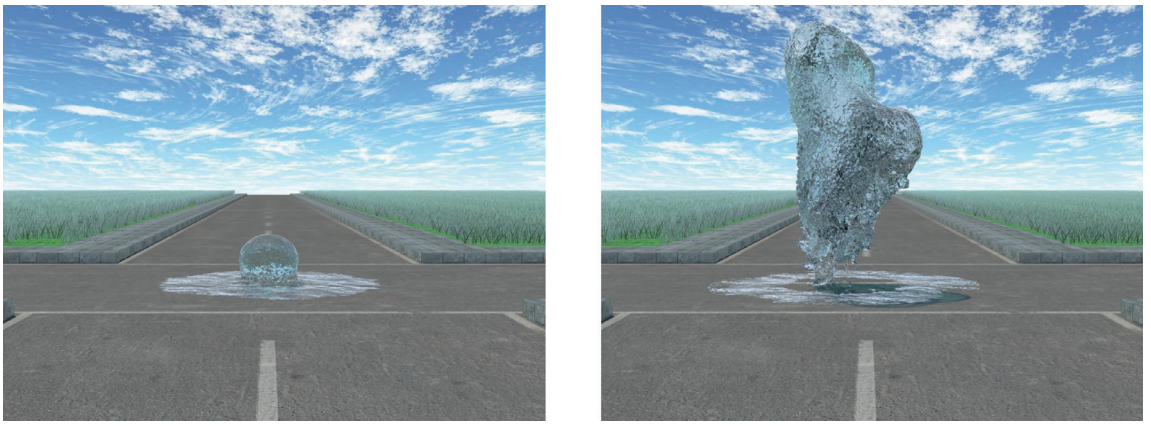

(a) t=2.375 s. (b) t=2.875 s.

Fig. 20. Geysering experiment, realistic plots.

Fig. 21. Frames from a footage of a geyser (https://www.youtube.com/watch?v=dM2L9EHNM5o).

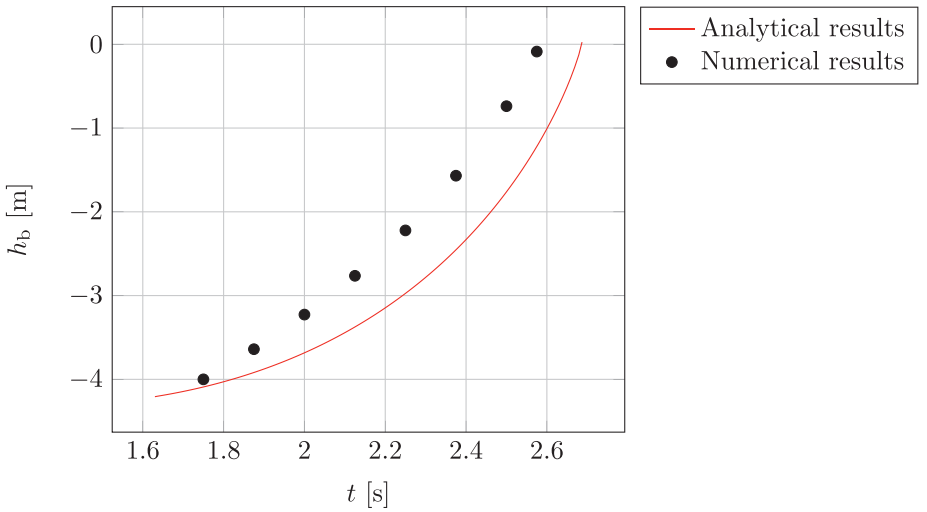

Fig. 22. Geysering experiment. Numerical and analytical results for bubble position in vertical duct.

6. Conclusions

Prevention of intrusion of air cavities into ducts appears to be a feasible solution to avoid geysering generation. Flow conditions under which air is not allowed to inflow into ducts determine minimum necessary flow rate in terms of duct slope and gate height. Whereas duct slope has a weak impact over the threshold flow rate, gate position plays an important role. For low gate heights, the flow limit requires velocities close to the celerity of air cavities (i.e. close to $0.464\sqrt{gd}$). Otherwise, for higher gate positions the threshold is related to the admissible flow rate over the gate. The strategy to determine these conditions proves to be effective for a realistic configuration and its future application for more complex geometries of sewer systems is encouraging.

The proposed semi-analytical approach succeeds in predicting dynamics of rising Taylor bubbles when gas expansion effects are significant. Although the model neglects some local characteristics of the flow such as detachment of small bubbles, time evolution of air cavity nose and free surface positions are accurately reproduced. Moreover, the simplified iterative solution procedure is very efficient and requires only a few seconds, in contrast to simulations based on finite element models, whose computational cost is of the order of hours or days. The theoretical formulation also predicts a sudden decompression of the bubble, which suffers a huge acceleration and violently drives the still water. Tests accomplished verify that if the analytical condition for sudden decompression is near to being fulfilled, bubble and free surface velocities greatly increase.

Generation and propagation of air cavities in conduits combine virtually-potential well-defined interfaces with diffuse zones having complex momentum exchange between air and water. Numerical experiments reveal that, although relative air pressure is small, expansion and compression of the bubble make weak-compressibility assumption necessary for an appropriate momentum transfer between fluids, including transitions between quasi-horizontal interface propagation and quasi-vertical direction. Three dimensional simulations (or at least axisymmetrical for circular tubes) are demanded for proper answers when air pressure reaches a level such that compression/expansion is not negligible. These requirements are common when vertical ducts are examined. The proposed numerical model for weakly compressible two fluid flows proves to be adequate to simulate these challenging problems of propagation of air cavities and geysering events, and supplements to a large degree available outputs of analytical approach, by providing details of the dynamics not well captured by theoretical procedure. In the case of simulations of multiple bubbles, the numerical model captures the effect of downstream wakes over trailing bubble, which alters moderately the expected bubble velocity given by semi-analytical model. On the other hand, for geysering experiments, full three dimensional numerical approach provides main topological features of the dynamics once water and air are expelled from the vertical duct, in agreement with observations. A challenging issue to be developed in the future is to couple returned jets with free surface depth integrated models for the ground level water propagation as an advanced numerical tool for integrated urban flooding studies.

Data Availability

The data has been included in the paper.

Acknowledgments

This work was supported by the Grant #PID2020-115778GB-I00 funded by MCIN/AEI/10.13039/ 501100011033. Open access charge was funded by Universidad de Granada / CBUA. Some figures have been plotted by using Paraview [42] and by an academic license of Autodesk 3ds Max [43].

Appendix A. A Brief on the Finite Element Solution

A1. High Order Solution

High order solution for mass conservation equation and momentum equation, Eqs. (7) and (2), respectively, is attained by extending the continuous characteristic based split FEM to incorporate preservation of second order accuracy for transient advective field condition (see Appendix A in Ref. [15]). After time discretization, the split method proposed can be written as the usual form,

$$\mathbf{u}^{n+1} = \mathbf{u}^{n} + \Delta\mathbf{u}^{*} + \Delta\mathbf{u}^{**}, \tag{52}$$

where velocity at time level $(n+1)\Delta t$ is computed as the sum of a predictor velocity $\mathbf{u}^{*} = \mathbf{u}^{n} + \Delta\mathbf{u}^{*}$, and a pressure correction velocity increment $\Delta\mathbf{u}^{**}$.

First step is the predictor velocity calculation, obtained by the Characteristic Galerkin method. Finite element discretization is stated in terms of the finite element spaces $\mathcal{U}_i^h$ and $\mathcal{V}_i^h$, i=1,d (d is the number of space dimensions), defined as

$\mathcal{V}_i^h \subset \mathcal{V}_i = \{v_i \in H^1(\Omega) \mid v_i = 0 \text{ on } \Gamma_q\}$, $\mathcal{U}_i^h \subset \mathcal{U}_i = \{u_i \in H^1(\Omega) \mid u_i = \overline{q}_i \text{ on } \Gamma_q\}$, where Γ_q is the portion of boundary with prescribed velocity, denoted as $\overline{\mathbf{q}}$. Solution is formulated as: Find $\Delta u_i^{*h} \in \mathcal{U}_i^h$ for all $t \in [t_o, T]$ such that

$$\begin{aligned}\left(v_i^h, \frac{\Delta u_i^{*h}}{\Delta t}\right)_\Omega &= -\left(v_i^h, \nabla\cdot\left(\left(\mathbf{u}^h\right)^{n+1/2}\left(u_i^h\right)^n\right)\right)_\Omega + \left(v_i^h, f_i^h\right)_\Omega^{n+1/2} + \left(v_i^h, g_i\right)_\Omega^n \\ &- \frac{\Delta t}{2}\Bigg\{\langle\nabla\cdot\left(v_i^h\left(\mathbf{u}^h\mathbf{u}^h\right)^{n+1/2}\right), \nabla\left(u_i^h\right)^n\rangle_{\Omega_l} - \langle v_i^h\left(\left(\mathbf{u}^h\right)^{n+1/2}\cdot\nabla\left(\mathbf{u}^h\right)^n\right), \nabla\left(u_i^h\right)^n\rangle_{\Omega_l} \\ &+ \left(\nabla\cdot v_i^h\left(\mathbf{u}^h\right)^{n+1/2}, \left(u_i^h\nabla\cdot\mathbf{u}^h\right)^n\right)_{\Omega_l} + \left(\nabla\cdot v_i^h\left(\mathbf{u}^h\right)^{n+1/2}, \left(u_i^h\nabla\cdot\mathbf{u}^h\right)^n\right)_{\Omega_l} \\ &+ \left(v_i^h, \left(\mathbf{u}^h\right)^{n+1/2}\cdot\left(\nabla\left(f_i^h + g_i\right)\right)^n\right)_{\Omega_l} + \left(\nabla\cdot v_i^h\left(\mathbf{u}^h\right)^{n+1/2}, \left(u_i^h\nabla\cdot\mathbf{u}^h\right)^n\right)_{\Omega_l}\Bigg\},\end{aligned} \tag{53}$$

where

$$(v, w)_\Omega = \int_\Omega v\, w\ \mathrm{d}\Omega\,, \quad \langle\mathbf{v}, \mathbf{w}\rangle_\Omega = \int_\Omega (\mathbf{v}\cdot\mathbf{w})\ \mathrm{d}\Omega \quad \text{and} \quad [v, \mathbf{c}]_\Gamma = \int_\Gamma v\,\mathbf{c}\cdot\mathbf{n}_b\ \mathrm{d}\Gamma,$$

$\mathbf{n}_b$ the outward unit normal to the boundary, Ω_l is the domain without elements with sides belonging to the boundary, and $\mathbf{f} = \frac{\mu}{\rho}\nabla^2\mathbf{u} + \mathbf{T} + \mathbf{Q}$. Supplemental integration by parts of viscous term (second term in the right hand side of Eq. (53)) is omitted for brevity.

Next step is the pressure computation from the continuity equation. Taking into account that $\mathbf{u}^{n+\theta_1} = \mathbf{u}^n + \theta_1(\Delta\mathbf{u}^* + \Delta\mathbf{u}^{**})$ and that $\Delta\mathbf{u}^{**}$ includes pressure terms, Eq. (7), after time discretization, is

$$\frac{1}{\left(a^2\right)^{n+1/2}}\frac{\Delta p}{\Delta t} - \theta_1\frac{\left(\rho^{'}\right)^{n+1/2}}{\rho^{n+1/2}}\Delta t\nabla^2\left(p^{n+\theta_2}\right) = -\nabla\cdot\left(\left(\rho^{'}\right)^n\mathbf{u}^n + \theta_1\left(\rho^{'}\right)^{n+1/2}\Delta\mathbf{u}^*\right), \tag{54}$$

where $p^{n+\theta_2} = (1-\theta_2)p^n + \theta_2 p^{n+1}$. Thus, Galerkin spatial discretisation of Eq. (54) is stated in terms of finite element spaces $\mathcal{W}^h$ and $\mathcal{P}^h$, defined as $\mathcal{W}^h \subset \mathcal{W} = \{w \in H^1(\Omega) \mid w = 0 \text{ on } \Gamma_p\}$, $\mathcal{P}^h \subset \mathcal{P} = \{p \in H^1(\Omega) \mid p = \overline{p} \text{ on } \Gamma_p\}$, where Γ_p specifies the portion of the boundary with prescribed pressure denoted as $\overline{p}$. Pressure solution is formulated as: Find $(p^h)^{n+1} \in \mathcal{P}^h$ for all $t \in [t_o, T]$, such that

$$\begin{aligned}&\left(\frac{1}{\left(a^2\right)^{n+1/2}}w^h, \frac{\Delta p^h}{\Delta t}\right)_\Omega + \theta_1\theta_2\Delta t\langle\nabla w^h, \frac{\left(\rho^{'}\right)^{n+1/2}}{\rho^{n+1/2}}\nabla\left(\Delta p^h\right)\rangle_\Omega = -\left(w^h, \nabla\cdot\left(\rho^{'}\mathbf{u}^h\right)\right)_\Omega^n \\ &+\theta_1\langle\nabla w^h, \left(\rho^{'}\right)^{n+1/2}\Delta\mathbf{u}^{*h}\rangle_\Omega - \theta_1\Delta t\langle\nabla w^h, \frac{\rho^{'}}{\rho}\nabla p^h\rangle_\Omega^n - \theta_1\left[w^h, \left(\rho^{'}\right)^{n+1/2}\Delta\mathbf{u}^h\right]_\Gamma,\end{aligned} \tag{55}$$

where $\Delta\mathbf{u}^h = (\mathbf{u}^h)^{n+1} - (\mathbf{u}^h)^n$. Values $\theta_1 = \theta_2 = 1$ are employed in numerical experiments.

Once pressure increment is computed, last step is to update the velocity field through the calculation of $\Delta\mathbf{u}^{**}$ by solving next equation

$$\left(v_i^h, \frac{\Delta u_i^{**h}}{\Delta t}\right)_\Omega = -\left(\frac{1}{\rho^{n+1/2}}v_i^h, \left(\nabla p^h\right)_i^{n+\theta_2}\right)_\Omega - \frac{\Delta t}{2}\left(\frac{1}{\rho^{n+1/2}}\nabla\cdot\left(v_i^h(\mathbf{u}^h)^{n+1/2}\right), \left(\nabla p^h\right)_i^{n+\theta_2}\right)_{\Omega_l}. \tag{56}$$

Finally, updated velocity field is computed by Eq. (52) and updated pressure field is $p^{n+1} = p^n + \Delta p$.

Solution of phase transport equation (Eq. (3)) is stated in terms of the finite element spaces $\mathcal{W}^h$ and Φ^h defined as $\mathcal{W}^h \subset \mathcal{W} = \{w \in H^1(\Omega) \mid w = 0 \text{ on } \Gamma_\phi^-\}$, $\Phi^h \subset \Phi = \{\phi \in H^1(\Omega) \mid \phi = \overline{\phi} \text{ on } \Gamma_\phi^-\}$, where Γ_ϕ^- specifies the portion of the boundary with prescribed phase function denoted as $\overline{\phi}$. Solution is formulated as: Find $\phi^h \in \Phi^h$ for all $t \in [t_o, T]$, such that

$$\begin{aligned}\left(w^h, \frac{\Delta\phi^h}{\Delta t}\right)_\Omega &= \left(\mathbf{u}^{n+1/2}\cdot\nabla w^h, \left(\phi^h\right)^n\right)_\Omega - \frac{\Delta t}{2}\Bigg\{\langle\nabla\cdot\left(w^h\left(\mathbf{u}^h\mathbf{u}^h\right)^{n+1/2}\right), \nabla\left(\phi^h\right)^n\rangle_{\Omega_l} \\ &-\langle w^h\left(\left(\mathbf{u}^h\right)^{n+1/2}\cdot\nabla\left(\mathbf{u}^h\right)^n\right), \nabla\left(\phi^h\right)^n\rangle_{\Omega_l} + \left(\nabla\cdot w^h\left(\mathbf{u}^h\right)^{n+1/2}, \left(\phi^h\nabla\cdot\mathbf{u}^h\right)^n\right)_{\Omega_l}\Bigg\} \\ &-\left[w^h, \phi^h\mathbf{u}\right]_{\Gamma^+}^n - \left[w^h, \overline{\mathbf{q}}_\phi\right]_{\Gamma_q^-}^n,\end{aligned} \tag{57}$$

where Γ_q^- is the portion of boundary with a prescribed inlet mass flux $\overline{\mathbf{q}}_\phi$, Γ^+ the portion of boundary with outlet condition ($\mathbf{u}\cdot\mathbf{n}_b > 0$), and $\phi^{n+1} = \phi^n + \Delta\phi$.

A2. Low Order Solution

Low order algorithm in NFEM is a finite element upwind method. Its application to the solution of Eqs. (1), (2), and (3) follows the same steps as the high order method. From now on, notation $\mathcal{LO}(\,)$ indicates the low order operator comprising computation of upwind fluxes. Reader can find a full derivation of the low order operator in Ref. [15], Section 3.3. Then, low order method is defined as: Find $(u_i^h)_{LO}^{n+1} \in \mathcal{U}_i^h$, $(i=1,d)$ and $(p^h)_{LO}^{n+1} \in \mathcal{P}^h$ for all $t \in [t_o, T]$, such that

$$\left(v_{iL}^h, \frac{\Delta u_{iLO}^h}{\Delta t}\right)_\Omega = \left(v_{iL}^h, \frac{\Delta u_{iLO}^{*h}}{\Delta t}\right)_\Omega - \left(v_{iL}^h, \frac{1}{\rho}\left(\nabla p^h\right)_{iLO}\right)_\Omega^{n+1/2}, \ (i=1,d), \tag{58}$$

where v_{iL}^h corresponds to the lumped mass matrix and *LO* subindex signifies low order solution.

Low order intermediate velocity increment is calculated as

$$\left(v_{iL}^h, \frac{\Delta u_{iLO}^{*h}}{\Delta t}\right)_\Omega = \left(v_i^h, f_i^h\right)_\Omega^n + \left(v_i^h, g_i\right)_\Omega^n + \mathcal{LO}\left((\mathbf{u}^h + \frac{\Delta t}{2}(\mathbf{f}^h + \mathbf{g}))^n, (\mathbf{u}^h)^n\right). \tag{59}$$

Pressure solution is nearly identical to high order formulation (Eq. (55)) and is not reproduced for brevity. Finally, the discrete low order form for phase function transport is formulated as: Find ϕ_{LO}^h such that

$$\left(w_L^h, \frac{\Delta \phi_{LO}^h}{\Delta t}\right)_\Omega = \mathcal{LO}\left((\phi^h)^n, (\mathbf{u}^h)^n\right), \tag{60}$$

where w_L^h corresponds to lumped mass matrix. We apply the low order upwind method in an edge-based manner for efficiency [15]. As mentioned before, full low order solution (58) is circumvented by an abridged version of the NFEM with only one computation of the pressure solution [12,14].

A3. Flux Correction Procedure

Considering a high order solution $\mathbf{B}$ and a low order predictor $\mathbf{b}$, flux correction techniques allow the computation of a corrected solution $\tilde{\mathbf{B}}$ that keeps the high order accuracy and maintains properties of the low order approach (e.g. positivity). Thus, corrected solution results from updating the low order solution at time $(n+1)\Delta t$ by the sum of corrected antidiffusive element contributions, denoted as $\mathbf{c}_j\mathbf{A}_j$,

$$\tilde{\mathbf{B}}_i^{n+1} = \mathbf{b}_i^{n+1} + \sum_{j=1}^{e} \mathbf{c}_j \mathbf{A}_j \,, \tag{61}$$

where $\mathbf{A}_j$ is the difference between contributions to node i of the high and low order schemes corresponding to element j, e is the number of elements j surrounding node i and $\mathbf{c}_j \in [0,1]$ are the elementwise correcting functions. These functions depend on the nodal high order solution at time $n\Delta t$, on the nodal low order solution at time $(n+1)\Delta t$, and on the element contribution to the node of the m variables of the problem (m=1 for Eq. (3) and $m = d+1$ for Eqs. (1) and (2)). Then, for $\mathbf{c}_j$=1 the corrected solution equals the high order solution, and for $\mathbf{c}_j$=0 solution equals the low order solution. Reader can consult Ref. [12] for a thorough description about the computation of the correcting functions.

Appendix B. Semi-Analytical Solution Algorithm

Solution of equations (21), (28) and (30) gives P_0, u_b and u_fs at time level t^{n+1}. A straightforward temporal discretization of the equations is,

$$\frac{P_0^{n+1}}{\rho_\mathrm{l}} = L_\mathrm{lc}\left[\left(\frac{\mathrm{d}u_\mathrm{fs}}{\mathrm{d}t}\right)^{n+1} + |g| + \frac{f}{2}\frac{u_\mathrm{fs}^{n+1}\left|u_\mathrm{fs}^{n+1}\right|}{D}\right], \tag{62}$$

$$u_\mathrm{fs}^{n+1} = \left(u_\mathrm{b}^{n+1} - U_\infty\right)\left(1 - \frac{\delta^*(D-\delta^*)}{D^2/4}\right) - \frac{4}{\pi D^2}\frac{V_\mathrm{g}}{\rho_\mathrm{g}}\frac{1}{\gamma C}\left(\frac{P_0^{n+1}+P_\mathrm{atm}}{C}\right)^{1/\gamma-1}\left(\frac{\mathrm{d}P_0}{\mathrm{d}t}\right)^{n+1}, \tag{63}$$

$$\beta\left(\frac{\mathrm{d}u_\mathrm{b}}{\mathrm{d}t}\right)^{n+1} = u_\mathrm{b}^{n+1}\alpha\rho_\mathrm{l}\psi\frac{V_\mathrm{g}}{\rho_\mathrm{g}}\frac{1}{\gamma C}\left(\frac{P_0^{n+1}+P_\mathrm{atm}}{C}\right)^{1/\gamma-1}\left(\frac{\mathrm{d}P_0}{\mathrm{d}t}\right)^{n+1} + |g|\rho_\mathrm{l}V_\mathrm{g} - \rho_\mathrm{l}\varepsilon V_\mathrm{g}\frac{u_\mathrm{b}^{n+1}\left|u_\mathrm{b}^{n+1}\right|}{D}. \tag{64}$$

Values of variables without superscript are considered at time level t^n. Derivative $(dB/dt)^{n+1}$ for a function $B(t)$ signifies

$$\left(\frac{\mathrm{d}B}{\mathrm{d}t}\right)^{n+1} = \begin{cases} \dfrac{3B^{n+1} - 4B^n + B^{n-1}}{2\Delta t} & if\ n > 0 \\ \dfrac{B^{n+1} - B^n}{\Delta t} & if\ n = 0 \end{cases}, \tag{65}$$

where $\Delta t = t^{n+1} - t^n$ and n=0 indicates initial time. Algorithm consists of the following steps:

1. Calculation of initial bubble parameters and liquid column length (ρ_g^0, V_b^0, δ^{*0}, ψ^0, L_b^0 and L_{lc}^0) for a duct geometry, gas mass and bubble position. At first time step $P_0^0 = L_{lc}^0|g|\rho_l$, u_{fs}^0=0, and u_b^0=0 or $u_b^0 = U_\infty$ are assumed.
2. Computation of P_0^{n+1}, u_b^{n+1} and u_{fs}^{n+1} for $n \geq 0$ by Eqs. (62), (63), and (64).
3. Free surface position updating,

$$h_{fs}^{n+1} = h_{fs}^n + u_{fs}^{n+1}\Delta t\,.$$

Note that $h_{fs}^{n+1} \leq H$, where H is the height of duct upper end.

4. Updating of ρ_g and V_g,

$$\rho_g^{n+1} = \left(\frac{P_0^{n+1} + P_{atm}}{C}\right)^{1/\gamma},$$

$$V_g^{n+1} = \frac{M_g}{\rho_g^{n+1}}\,.$$

5. Bubble shape recalculation: L_b^{n+1}, δ^{*n+1}.
6. Updating of L_{lc},

$$L_{lc}^{n+1} = L_{lc}^n + \Delta t\left(u_{fs}^{n+1} - u_b^{n+1} - \frac{4\psi^{n+1}}{\pi D^2}\left(\frac{-V_g}{\rho_g}\right)^{n+1}\frac{1}{\gamma C}\left(\frac{P_0^{n+1} + P_{atm}}{C}\right)^{1/\gamma-1}\left(\frac{dP_0}{dt}\right)^{n+1}\right);$$

if free surface has reached the upper end of the duct, L_{lc}^{n+1} is computed as

$$L_{lc}^{n+1} = L_{lc}^n + \Delta t\left(-u_b^{n+1} - \frac{4\psi^{n+1}}{\pi D^2}\left(\frac{-V_g}{\rho_g}\right)^{n+1}\frac{1}{\gamma C}\left(\frac{P_0^{n+1} + P_{atm}}{C}\right)^{1/\gamma-1}\left(\frac{dP_0}{dt}\right)^{n+1}\right).$$

7. Calculation of bubble nose position h_b,

$$h_b^{n+1} = h_{fs}^{n+1} - L_{lc}^{n+1}\,.$$

8. If $h_b^{n+1} < h_{fs}^{n+1}$, return to step 2.

Supplementary material

Supplementary material associated with this article can be found, in the online version, at 10.1016/j.apm.2022.06.016

References

[1] T.B. Benjamin, Gravity currents and related phenomena, J. Fluid Mech. 31 (1968) 209–248.
[2] D.L. Wilkinson, Motion of air cavities in long horizontal ducts, J. Fluid Mech. 118 (1982) 109–122.
[3] H. Bashiri-Atrabi, T. Hosoda, Assessment of two-equation model for simulation of air pocket advancing into a rectangular duct, J. Hydraul. Res. 57 (2019) 122–130.
[4] O.E. Coronado-Hernández, V.S. Fuertes-Miquel, P.L. Iglesias-Rey, F.J. Martínez-Solano, Rigid water column model for simulating the emptying process in a pipeline using pressurized air, J. Hydraul. Eng. 144 (2018) 06018004.
[5] L. Wang, F. Wang, B. Karney, A. Malekpour, Numerical investigation of rapid filling in bypass pipelines, J. Hydraul. Res. 55 (2017) 647–656.
[6] L. Zhou, H. Wang, B. Karney, D. Liu, P. Wang, S. Guo, Dynamic behavior of entrapped air pocket in a water filling pipeline, J. Hydraul. Eng. 144 (2018) 04018045.
[7] S.N. Chan, J. Cong, J.H. Lee, 3d numerical modeling of geyser formation by release of entrapped air from horizontal pipe into vertical shaft, J. Hydraul. Eng. 144 (2018) 04017071.
[8] V.S. Fuertes-Miquel, O.E. Coronado-Hernández, D. Mora-Meliá, P.L. Iglesias-Rey, Hydraulic modeling during filling and emptying processes in pressurized pipelines: a literature review, Urban Water J. 16 (2019) 299–311.
[9] M. Cruchaga, L. Battaglia, M. Storti, J. D'Elía, Numerical modeling and experimental validation of free surface flow problems, Arch. Comput. Methods Eng. 23 (2016) 139–169.
[10] E. Olsson, G. Kreiss, A conservative level set method for two phase flow, J. Comput. Phys. 210 (2005) 225–246.
[11] E. Olsson, G. Kreiss, S. Zahedi, A conservative level set method for two phase flow II, J. Comput. Phys. 225 (2007) 785–807.
[12] J. Molina, P. Ortiz, A conservative flux–corrected continuous FEM for fluid interface dynamics, Int. J. Numer. Methods Fluids 91 (2019) 287–310.
[13] J.C. Cano-Lozano, R. Bolaños Jiménez, C. Gutiérrez-Montes, C. Martínez-Bazán, The use of volume of fluid technique to analyze multiphase flows: Specific case of bubble rising in still liquids, Appl. Math. Model. 39 (2015) 3290–3305.
[14] J. Molina, P. Ortiz, A continuous finite element solution of fluid interface propagation for emergence of cavities and geysering, Comput. Methods in Appl. Mech. Eng. 359 (2020) 112746.
[15] P. Ortiz, A positive definite continuous FEM model for advection, Adv. Water Resour. 32 (8) (2009) 1359–1371.
[16] P. Ortiz, Non-oscillatory continuous FEM for transport and shallow water flows, Comput. Methods in Appl. Mech. Eng. 223–224 (2012) 55–69.
[17] P. Ortiz, Shallow water flows over flooding areas by a flux-corrected finite element method, J. Hydraul. Res. 52 (2014) 241–252.
[18] R. Löhner, C. Yang, E. Oñate, On the simulation of flows with violent free surface motion, Comput. Methods in Appl. Mech. Eng. 195 (2006) 5597–5620.
[19] W.D. Baines, Air cavities as gravity currents on slope, J. Hydraul. Eng. 117 (1992) 1600–1615.
[20] P.R. Garabedian, On steady-state bubbles generated by taylor instability, P. Roy. Soc. A - Math. Phy. 241 (1957) 423–431.
[21] K.H. Bendiksen, On the motion of long bubbles in vertical tubes, Int. J. Multiph. Flow 11 (1985) 797–812.

[22] J.G. Vasconcelos, S.J. Wright, Geysering generated by large air pockets released through water-filled ventilation shafts, J. Hydraul. Eng. 137 (2011) 543–555.
[23] O. Zienkiewicz, R. Taylor, P. Nithiarasu, The finite element method for fluid dynamics, 7th Edition, Butterworth-Heinemann, Oxford, 2014.
[24] J.U. Brackbill, D.B. Kothe, C. Zemach, A continuum method for modeling surface tension, J. Comput. Phys. 100 (1992) 335–354.
[25] P. Ortiz, J. Anguita, M. Riveiro, Free surface flows over partially erodible beds by a continuous finite element method, Environ. Earth Sci. 74 (2015) 7357–7370.
[26] P. Ortiz, O. Zienkiewicz, J. Szmelter, Hydrodynamics and transport in estuaries and rivers by the CBS finite element method, Int. J. Numer. Meth. Eng. 66 (2006) 1569–1586.
[27] T.R. Nigmatulin, F.J. Bonetto, Shape of taylor bubbles in vertical tubes, Int. Comm. Heat Mass Transfer. 24 (1997) 1177–1185.
[28] D.T. Dumitrescu, Strömung an einer luftblase im senkrechten rohr, Z. Angew. Math. Mech. 24 (1943) 139–149.
[29] D.J. Nicklin, Two-phase flow in vertical tubes, Trans. Inst. Chem. Engr. 40 (1962) 61–68.
[30] G. Batchelor, An Introduction to Fluid Dynamics (Cambridge Mathematical Library), Cambridge University Press, 2000.
[31] S. Nogueira, M.L. Riethmuler, J.B.L.M. Campos, A.M.F.R. Pinto, Flow in the nose region and annular film around a taylor bubble rising through vertical columns of stagnant and flowing newtonian liquids, Chem. Eng. Sci. 61 (2008) 845–857.
[32] L. Cheng, G. Ribatski, J.R. Thome, Two-phase flow patterns and flow-pattern maps: fundamentals and applications, Appl. Mech. Rev. 61 (5) (2008) 1–28.
[33] J. Li, A. McCorquodale, Modeling mixed flow in storm sewers, J. Hydraul. Eng. 125 (1999) 1170–1180.
[34] R.G. Sousa, A.M.F.R. Pinto, J.B.L.M. Campos, Effect of gas expansion on the velocity of a taylor bubble: PIV measurements, Int. J. Multiph. Flow 32 (2006) 1182–1190.
[35] A.A. Kendoush, The virtual mass theory of a taylor bubble rising in vertical pipes, J. Fluids Eng. 140 (2018) 051202.
[36] V. Baumbach, E. Hopfinger, A. Cartellier, The transient behaviour of a large bubble in a vertical tube, J. Fluid Mech. 524 (2005) 131–142.
[37] C.A. Talvy, L. Shemer, D. Barnea, On the interaction between two consecutive elongated bubbles in a vertical pipe, Int. J. Multiph. Flow 26 (2000) 1905–1923.
[38] A.S. Leon, I.S. Elayeb, Y. Tang, An experimental study on violent geysers in vertical pipes, J. Hydraul. Res. 57 (2019) 283–294.
[39] X. Chen, N. Chen, A. Delgado, Numerical study of formation of a series of bubbles at a submerged orifice, Appl. Math. Model. 73 (2019) 668–694.
[40] A. Smolianski, H. Haario, P. Luukka, Numerical study of dynamics of single bubbles and bubble swarms, Appl. Math. Model. 32 (2008) 641–659.
[41] C. Song, Y. Pan, P. Ma, M. Zhao, T. Liu, Numerical simulation on the influence of submerged combustion on splashing and heat transfer in TSL furnace, Metals 12 (2022) 328.
[42] Paraview, open source visualization, 2014, http://www.paraview.org.
[43] Autodesk 3ds max (2016). https://www.autodesk.com/products/3ds-max/overview